A quarter-century of H-mode studies

2007 Plasma Phys. Control. Fusion 49 B1

(http://iopscience.iop.org/0741-3335/49/12B/S01)

IOP PUBLISHING PLASMA PHYSICS AND CONTROLLED FUSION

Plasma Phys. Control. Fusion **49** (2007) B1–B33 doi:10.1088/0741-3335/49/12B/S01

A quarter-century of H-mode studies

F Wagner

Max-Planck-Institut für Plasmaphysik, Teilinstitut Greifswald, EURATOM Association, D-17489 Greifswald, Germany

E-mail: fritz.wagner@ipp.mpg.de

Received 6 July 2007
Published 14 November 2007
Online at stacks.iop.org/PPCF/49/B1

Abstract

The H-mode is a confinement mode of toroidal plasmas, which may make the goals of fusion possible—the development of a clean energy source at competitive electricity costs. The most challenging aspect of the H-mode physics is the sudden disappearance of the edge turbulence whereas its driving forces—the gradients—increase. As the physics behind the H-mode is subtle many features are not yet clarified. There is, however, substantial experimental and theoretical evidence that turbulent flows, which normally limit the confinement, are diminished by sheared poloidal flow residing at the plasma edge. There are many conceivable mechanisms giving rise to sheared flow. The most intriguing of these is that fluctuations themselves induce the flow, which acts back to its generating origin and annihilates the turbulence. This review concentrates mostly on the transition physics, describes one line of understanding the H-mode in more detail, recalls some of the older observations and summarizes the achievements in the H-mode for both tokamaks and stellarators.

(Some figures in this article are in colour only in the electronic version)

1. The initial years of H-mode studies

The H-mode was discovered 25 years ago [1] at the 'old' ASDEX, which is operated now as HL-2A at SWIP in China [2]. Figure 1 shows two density traces (n_e), one of an L-mode and one of an H-mode discharge taken shortly after the H-mode discovery, 4 February 1982[1]. The external parameter of the two discharges of figure 1, which decided which mode developed during the neutral injection phase (NBI), was the selected target density of the ohmic phase. The density drop in the L-mode was caused by a reduction of the particle confinement from the ohmic level; in the H-mode, particle confinement improved again leading to a steep rise in n_e. The importance of the H-mode was obvious from the very beginning because the energy content increased substantially at constant heating power.

[1] Initially, the two discharge types were called a and b discharges, which was mnemonically not very clever and was quickly changed.

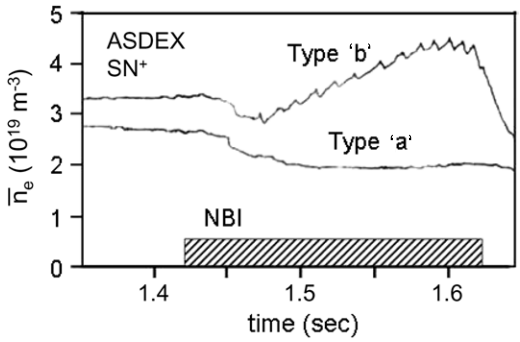

Figure 1. Line average density traces from an L-mode discharge (dubbed Type 'a' for historical reasons) and an early H-mode discharge (Type 'b'). The window of NBI heating is indicated. The configuration was SN^+ (ion-grad-B drift towards the X-point).

The following observations were made in the initial H-mode campaigns:

(1) L- and H-modes differ in confinement time by about a factor of two: two operational branches exist for a given setting; the space in between is not accessible.
(2) Energy-, particle-, impurity- and momentum transport improve simultaneously.
(3) The H-mode transition requires a minimal heating power: obviously, a critical condition, the power threshold P_{th}, has to be met.
(4) There is a dwell-time after the heating power has been increased from the ohmic level, before the plasma transits into the H-phase. The dwell-time depends on external parameters and is shorter at higher power. It also depends strongly on the magnetic configuration and can be shorter under single- instead of double-null configuration (see section 6.2).
(5) When the heating power has been switched off, the plasma remains in the H-phase for a dwell-time on the order of the confinement time: after the forward L–H transition, the plasma does not hover at the transition condition but moves deeper into the H-mode domain; when the external drive is turned off, this reserve allows the plasma to initially remain in the H-phase. Of significance is that the back transition is not gradual but also occurs in a distinct step—corresponding to the gap between the H- and L-mode branches.
(6) There is also a density threshold; at low density, the critical transition condition cannot be met. Later it was observed that machine characteristics like radiation and mode-locking affect the low-density power threshold [3].
(7) Large sawteeth were found to trigger the H-mode: the critical transition parameter seems to be a local condition at the plasma edge, which can be met by a thermal wave from the core plasma.
(8) ELMs appeared in the H-mode as a new type of edge localized MHD instability [4]; there are operational ways to suppress ELMs. In the quiescent H^*-mode the intrinsic confinement of the H-mode can be studied. This regime is, however, normally transient due to a continuous increase of impurity concentration (see also section 9.3).

The power threshold was found to be lower for the following cases:

(9) With separatrix instead of limiter operation.
(10) In deuterium instead of hydrogen plasmas; the actual value of P_{th} depends on the isotopic mix.
(11) In clean (with boronization) instead of dirty plasmas.

(12) With gas fuelling from the divertor chamber or the high-field side instead of the low-field side. These aspects entered later into the discussion of the impact of divertor closure on τ_E and $P_{\rm th}$ [5].

(13) In single-null (SN) plasmas with the ion-grad B-drift to (SN^+) instead of away (SN^-) from the active X-point; in double-null (DN) plasmas, $P_{\rm th}$ was found to lie in between [6]: obviously, an unknown mechanism (see section 6.2) whose impact is formally expressed as ion ($B \times \nabla B$)-drift direction in relation to the X-point location, contributes with a supporting (or prohibiting, respectively) effect, which was nullified in ASDEX in the symmetric DN case. At a heating power, sufficient to get the H-mode under DN conditions, the dwell-time prior to the transition is shortened by about a factor of two if operated under SN^+ conditions (see figure 101 of [7]). Under SN^- conditions, the dwell-time could exceed the NBI pulse length.

Later the H-mode could also be realized (as transition) with ICRH [8]. In this case the H-transition occurred without additional toroidal momentum input. The H-mode was reproduced in 1984 in PDX [9], in 1986 in DIII-D [10] and in 1987 in JET [11]. Finally, in 1993, the first H-mode transition was achieved in the W7-AS stellarator demonstrating that the H-mode is a generic feature of toroidal confinement [12]. Whereas the H-mode came as an unexpected event in ASDEX ('Das Wesentliche an jeder Erfindung tut der Zufall ...', Friedrich Nietzsche), we had enough recipe-like understanding as described above to develop it in W7-AS in a targeted process (separatrix, boronization, high-power, high-density) first with electron cyclotron resonance heating (ECRH) and later with neutral beam injection (NBI) heating [13]. Generally, H-mode operation initiated a learning process with the result that $P_{\rm th}$ continuously dropped and the operational space expanded. Nowadays, the H-mode is the favoured operational regime. To date, the largest fusion power has been achieved in the H-mode [14] and the ITER design is based on it [15]. The evolution of the H-mode understanding is covered in several review papers [7, 16–23].

2. Stellarator H-mode

Figure 2 shows as a tableau the variation of global and edge plasma parameters at the L–H transition. Results from the W7-AS stellarator [24] are plotted, which are quite typical for the transition. Figure 2(a) shows the H_α-trace with the distinct transition into an ELM-free phase; figure 2(b), the energy content ($W_{\rm dia}$) and the global radiation; figure 2(c), the line average density and two density traces at the plasma edge (the separatrix is at $r_{\rm eff} = 14$ cm); figure 2(d), two edge $T_{\rm e}$-traces (ECE; the traces terminate at cut-off), figure 2(e), three edge $T_{\rm i}$ traces; figure 2(f), the radial electric field variation at the edge and figure 2(g) shows logarithmically the scattered power from reflectometry P_n ($k_\theta \sim$ 6–10 cm^{-1}; $n_{\rm cutoff} = 2 \times 10^{13}$ cm^{-3}). The H-mode transition has a strong impact on all plasma parameters—on global ones like the energy and particle content and the plasma radiation, and—more distinct—on the local edge parameters. All parameters establishing the local pressure gradient increase. Of specific importance is the sharp decrease of the fluctuation activity simultaneously with that of the edge electric field towards more negative values.

The implication of the H-mode in W7-AS (and heliotrons [25]) for H-mode and ELM theories is quite substantial. The separatrix of W7-AS has a finite value of the rotational transform iota whereas in divertor tokamaks, $\iota => 0$ at the separatrix; the global magnetic shear at the edge is distinctively lower than for a typical tokamak by a factor of about 10. This might be of relevance for Kelvin–Helmholtz instabilities in the case of strong plasma flows. The stellarator-tokamak comparison might indicate that the toroidal current, the large edge-q

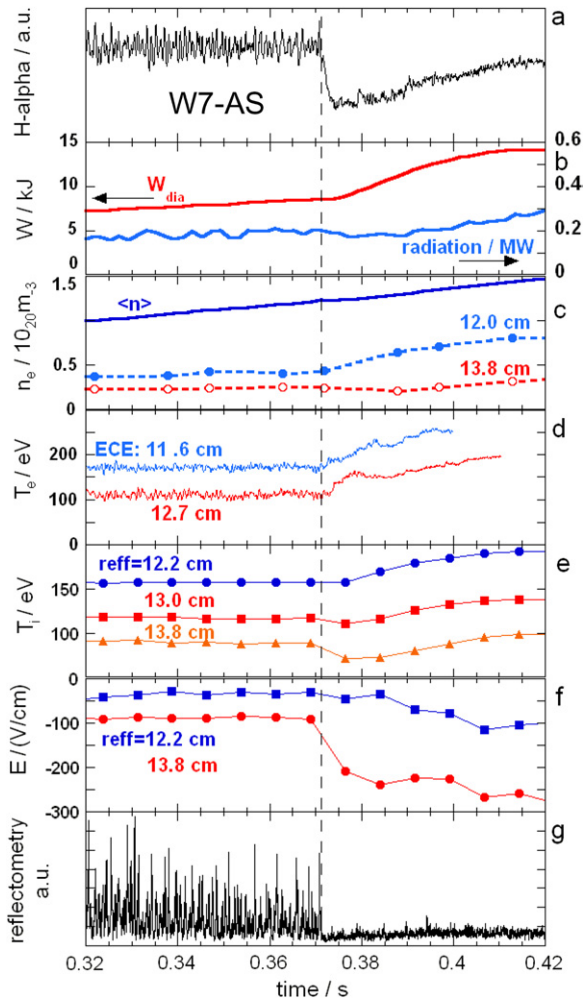

Figure 2. This tableau shows an L–H transition in W7-AS (NBI); the transition is indicated by the vertical line. (*a*) H_α-radiation with the characteristic transition mark; (*b*) energy content $W_{\rm dia}$ and global radiation; (*c*) line average density and two edge density traces; (*d*) edge $T_{\rm e}$ traces; the lines stop at the density cut-off; (*e*) edge $T_{\rm i}$ traces; (*f*) two edge traces showing the radial electric field E_r; (*g*) scattered power from edge reflectometry.

and strong global magnetic shear of divertor tokamaks, magnetic hill or well may play, to first order, a minor role in the transition physics.

The intrinsic ambipolarity of the neoclassical particle fluxes ($\langle j_r \rangle = 0$ independent of E_r) is not ensured in 3D systems by angular momentum conservation as in tokamaks but instead the radial electric field E_r is enforced by $\Gamma_{\rm e} = \Gamma_{\rm i}$. As a consequence, bifurcating solutions for E_r are a known feature of stellarator transport (an experimental summary is given in [26]). Another effect of the 3D geometry of helical systems is the strong toroidal flow damping.

W7-AS does show ELMs whose activity increases with heating power. There is no net induced toroidal current of substantial value to drive ELMs. The edge bootstrap current—also a potential drive for ELMs—is low owing to the high edge collisionality as the H-mode of W7-AS is generally observed at elevated densities.

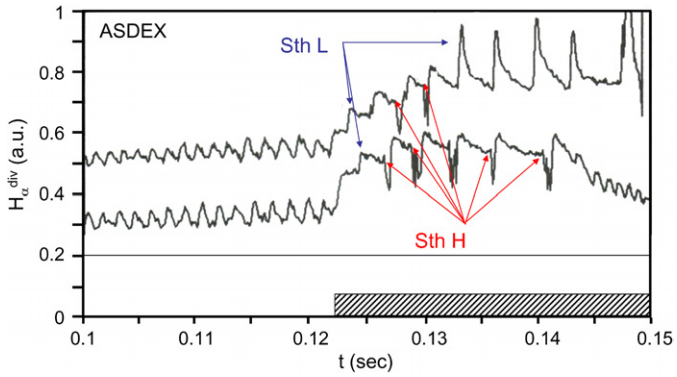

Figure 3. H_α of two L-mode discharges (from OH into NBI heating). The traces are modulated by sawteeth in the ohmic phase. The sawtooth amplitude increases in the auxiliary heating phase (Sth L) apart from those pulses which induce a short H-mode (Sth H). Some of these H-mode periods show ELMs.

Also in W7-AS the plasma remains in the H-phase for a short period after the heating pulse has been switched off (see figure 14). The post-beam-pulse (PBP) dwell-time is of the order of the confinement time. With $\tau_E^{\mathrm{H}}/\tau_E^{\mathrm{L}} \sim 2$, $\Delta t_{\mathrm{H\text{–}L}} \sim -\tau_E \ln \tau_E^{\mathrm{L}}/\tau_E^{\mathrm{H}} \sim -\tau_E \ln 0.5$. Both for ASDEX and W7-AS, $\Delta t_{\mathrm{H\text{–}L}}/\tau_E \sim 0.57$ (ASDEX: $\tau_E = 67$ ms; $\Delta t_{\mathrm{H\text{–}L}} = 38$ ms. W7-AS: $\tau_E = 28$ ms; $\Delta t_{\mathrm{H\text{–}L}} = 16$ ms).

Major differences to the tokamak H-modes seem to be the low power threshold ($P_{\mathrm{th}}^{\mathrm{W7AS}}/P_{\mathrm{th}}^{\mathrm{TOKscal}} < 1/2$) and the limitation of the H*-mode to specific iota windows (see section 6.3).

3. Initial understanding of the H-mode transition physics

3.1. Transition related observations

The identification of the critical transition parameter(s) turned out to be rather difficult. Right at the transition, we could compare on ASDEX all diagnostically accessible parameters of a discharge exhibiting an H-mode transition with one of the same external settings, which remained in the L-phase (see figure 67 in [7]). No resolvable difference could be noted right at the bifurcation point to the H-mode branch. One has to acknowledge, of course, that the diagnostic equipment then did not have today's sophistication.

The observations (3)–(5), (7), (9), (11)–(13) indicated that the transition condition could develop from an energy balance governed by sources, sinks and transport: the critical conditions are met in the course of the heating phase if enough power is available. At higher heating power, the transition occurs earlier. After the heating pulse, the equilibrium evolves in the reverse direction and the back transition occurs. Sinks in the energy balance are impurity radiation (e.g. an H-mode is not possible with an edge Marfe) (11), recycling located right at the plasma surface (9) or at the sensitive low-field zones where the turbulence growth rate is largest (12). Also the $B \times \nabla B$ drift effect on P_{th} (13) was originally understood in terms of the ion power balance: the neoclassical effect of a poloidally distributed heat sink reduces or increases the heat flux for a given ∇T_{i} in collisional plasmas depending on the drift of the ion to or away from the X-point as sink [27].

Direct evidence that the critical transition condition is local and resides at the plasma edge came from the observation of sawtooth-triggered H-phases. Figure 3 shows H_α-traces of two L-mode discharges with P just below P_{th} displaying the signal variation with sawteeth in the

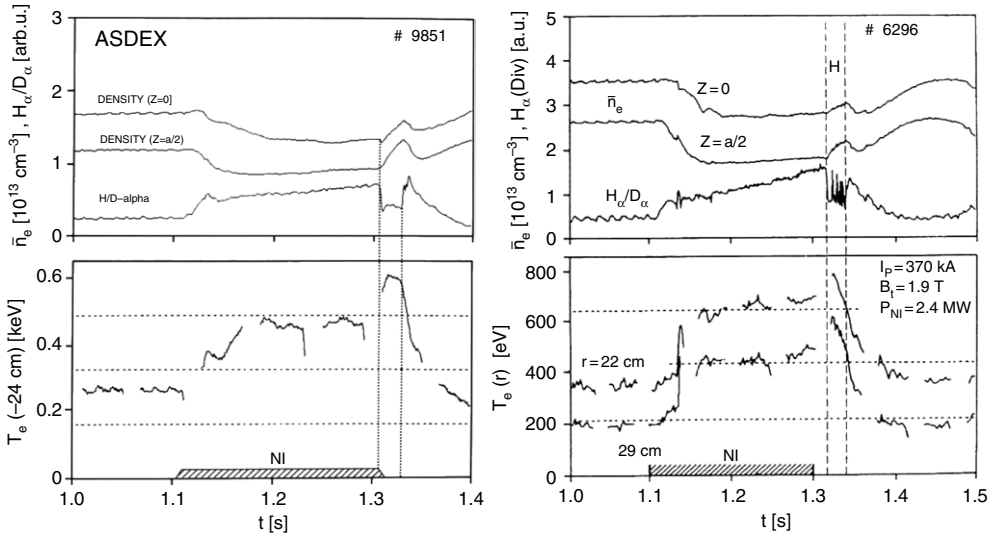

Figure 4. Two discharges which stay in the L-mode during NBI but display short H-phases after the beams have been switched off. Upper traces: line averaged densities (central chord; half-way to the edge) and H_α-trace. Lower curves: T_e (ECE) close to the edge (the traces are interrupted to monitor the background). The H-transitions occur during the PBP T_e rise. The left case shows a quiescent, the right case an ELMy PBP H-phase.

L-phase (signal transiently increases) and when short H-phases were triggered—even with ELMs. The H-phases initiate an H_α-signal drop. In the lower case, each sawtooth triggers a short H-phase (apart from the first one after NBI has been started).

A remarkable observation has been that L-mode plasmas could turn into an H-mode after (!) the NBI heating power has been switched off. This phase is characterized by an adjustment of the plasma equilibrium—the plasma moves by $\Delta R/R \sim -1\%$ towards higher field, and—with NBI—by the post-beam-pulse (PBP) electron temperature rise [28]. Figure 4 shows two such cases—one without, one with ELMs. T_e rises because the cold electron flux, introduced by the beams, is suddenly turned off. This case again showed that local heating (actually the loss of local cooling) causes the transition and it pointed to the role of T_e (edge) as a possible crucial control parameter. I am aware of post-heating-pulse H-modes only in conjunction with NBI.

The isotopic effect on P_{th} seems to be evidence for the role of transport in the power balance, which establishes the critical edge condition. In ASDEX, we observed a strong isotopic effect in transport [29] with deuterium yielding the better confinement. Lower transport in D-plasmas obviously allows meeting the critical H-mode transition parameters at lower heating power. This trend continued to tritium-plasmas of JET [30]. On the other hand, stellarator plasmas do not show an obvious isotopic effect in confinement and—lo and behold—also the power threshold does not depend on the isotopic mass. The conclusion from the different tokamak-stellarator behaviour could be that P_{th} is indeed affected by the local transport and that the isotopic effect is introduced by this characteristic feature of turbulent transport.

Also the hysteresis in P_{th}—the H-mode, when established, allows a reduction of the heating power by a factor of two below P_{th} [31]—could be explained by confinement. One asymmetry between the L–H and the H–L back transition is that they occur from the L-mode or the H-mode confinement level, respectively.

The impact of sources, sinks and transport on P_{th} indicated already that the critical parameter must be linked more to plasma gradients than to scalar parameters.

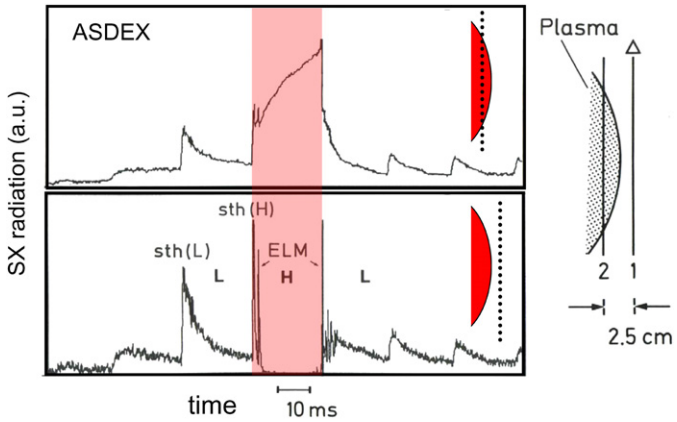

Figure 5. Transitions from OH to NBI heating. Shown are two soft-x-ray traces one inside the separatrix and the other in the SOL (see schematics at the right). The two signals are modulated by sawteeth with initially rising amplitude. The 4th sawtooth causes an H-transition developing a transport barrier at the edge. The short H-phase displays an ELM.

3.2. Development of an edge transport barrier

The sawtooth-triggered H-mode helped to understand one important aspect of the H-mode that the improved confinement is caused by the development of a transport barrier right at the edge but inside the separatrix [32]. Figure 5 shows a sequence of sawteeth at the transition from the ohmic to the NBI heating phase. The upper trace viewed the plasma right inside the separatrix, the lower one predominantly the SOL plasma (see geometry on the right side). Auxiliary heating caused the sawtooth amplitude to initially increase. The need to overcome the power threshold translates into a critical sawtooth amplitude and when this is met (with the sawtooth labelled sth(H)), a short H-phase develops. Whereas the sawteeth in the preceding and succeeding L-phases cross the separatrix and also modulate the SX radiation emerging from the SOL, the sawtooth, which triggers a short H-phase, causes the SX signal from inside the separatrix to steadily increase at the expense of the signal from the SOL, which collapses: an edge transport barrier has been developed.

The gradual development of the edge profiles—that of the density is shown in figure 6 [33]—allowed assessment of the reduction in heat diffusivities within the transport barrier (for the ions approximately to the level of neoclassical heat diffusivity, for the electrons still above it). With far-infrared laser scattering, we could show that the level of turbulence dropped sharply right at the formation of the transport barrier [34].

Figure 7 shows the collapse of the turbulent particle flux Γ in DIII-D as a consequence of the H-transition [35]. Γ was deduced from edge density and potential fluctuations using Langmuir probes. To safely employ this tool, the study had been carried out in H-transitions of low power ohmic discharges. The results demonstrate that the confinement improvement of the H-mode is indeed caused by a reduction of turbulent fluxes.

The two traces in figure 1 already address the nature of the H-mode transition as a bifurcation. In the H-mode case the density increased although the external gas flow was terminated; in the L-mode case the density decreased even though the external gas flow was strongly increased by the gas feed-back system. The space between these density branches was not accessible.

The question of the true nature of the transitions (L–H and H–L) actually arises because normally, the transitions are enforced by large jumps in auxiliary heating power. It is interesting

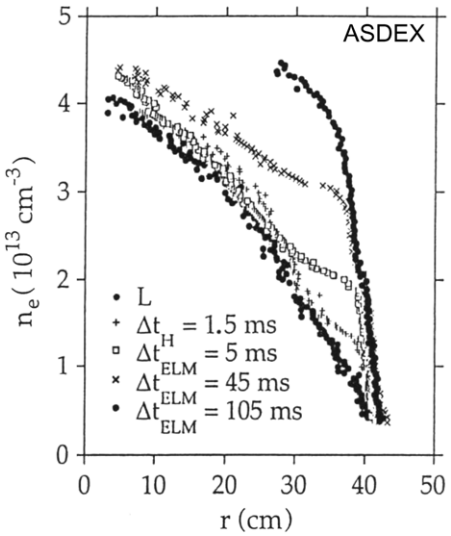

Figure 6. Development of the density profile after H-transition [33].

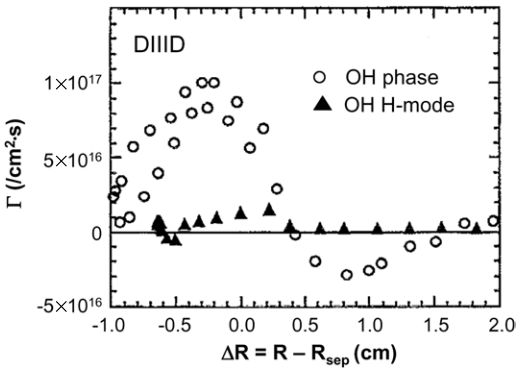

Figure 7. Turbulent particle flux Γ at the plasma edge for ohmically heated discharges—with/without an H-mode. Γ is measured around the separatrix. The data are from DIII-D [35]. Reprinted with the permission of AIP.

in this context that sawtooth-triggered H-phases or the PBP H-phases emerge without strong external drive: in one case the external power is on and slightly below P_{th}, and in the other case, the heating power even decreases within the ion-slowing down phase. In W7-AS, the H-mode is generally initiated at constant heating power by slowly increasing the density (see figure 2). In this case the evolution remains close to transport equilibria. All these H-modes evolve more out of internal adjustment processes. Nevertheless, the formation or destruction of the transport barrier occurs in a distinct step (see section 5.2).

Often, the H-transition evolves in a sequence of limit-cycle oscillations. This specific phenomenon of bifurcating states is well documented in tokamaks [36, 37]; therefore, figure 8(*a*) shows a case from W7-AS. The transition is characterized by dithers, which gradually transmute to ELMs. Also in this case, the plasma jumps between the two states—the L- and the H-mode branches. It is an interesting question, which of the transitions is the last

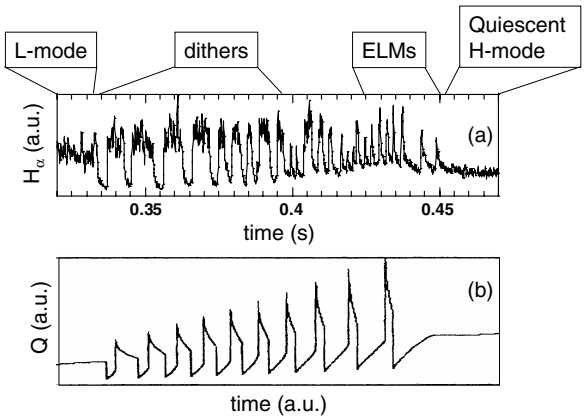

Figure 8. (*a*) Dithering cycle of a slow L–H transition shown by H_α radiation; (*b*) model of a dithering transition from [36]. Reprinted with the permission of the American Physical Society.

dither (a bifurcation phenomenon), which the first ELM (MHD instability). The interspersed L-phases of the dithering cycle are characterized by strong, intermittent, ELM-like turbulence.

The H_α trace of figure 8(*a*) is reminiscent of the modelled temporal evolution of the power flux across the separatrix from Zohm [36], shown in figure 8(*b*). The model is based on the conception that the transition initiates two competing processes—one which would stabilize the H-mode, the other which would lead back to the L-mode. As the H-mode improves energy and particle confinement, one can construct a corresponding model based on τ_E, stabilizing the H-mode and on the consequences of an increase of τ_p, leading toward the L-mode. These two quantities would also involve two different time scales as the source for the energy content is in the core whereas that for the particles resides at the edge.

The duration of the L-phases in figure 8(*b*) drops from about 6 to 2 ms, which qualitatively fits the model; the duration of the H-phase stays rather constant at about 3 ms and prolongs in a later phase, interrupted by ELMs; finally a quiescent phase develops. If we interpret the dwell-time of the short H-phases as edge confinement time in the H-mode, the inherent diffusivity is $D \sim 0.3\,\mathrm{m^2\,s^{-1}}$.

4. The role of the radial electric field at the plasma edge

4.1. The development of an edge E_r-field well

The potential role of the edge radial electric field E_r in the evolution of the transport barrier was first introduced by Itoh and Itoh [38] actually before the first experimental observations were available. They recognized the H-transition as a bifurcation and constructed E_r-based bifurcation models to describe L- and H-mode branches. They conjectured that the losses of those ions at the edge which satisfy the toroidal resonance are not completely balanced by turbulent electron fluxes because of wave momentum losses across the plasma boundary.

It was left to the excellent edge diagnostics of DIII-D and to Burrell [39] and Groebner [40] to first measure E_r at the edge and to link it to the local turbulence suppression (see also [41]). Figure 9 shows the development of an E_r-field well right at the edge and right after the transition both for W7-AS (figure 9(*a*)) [42–44] and for ASDEX-Upgrade (figure 9(*b*)) [45]. In the radial range of the well the fluctuations are quenched, the turbulent transport decreases and steep gradients develop. Three remarks are appropriate: (1) the formation of an E_r-field well right

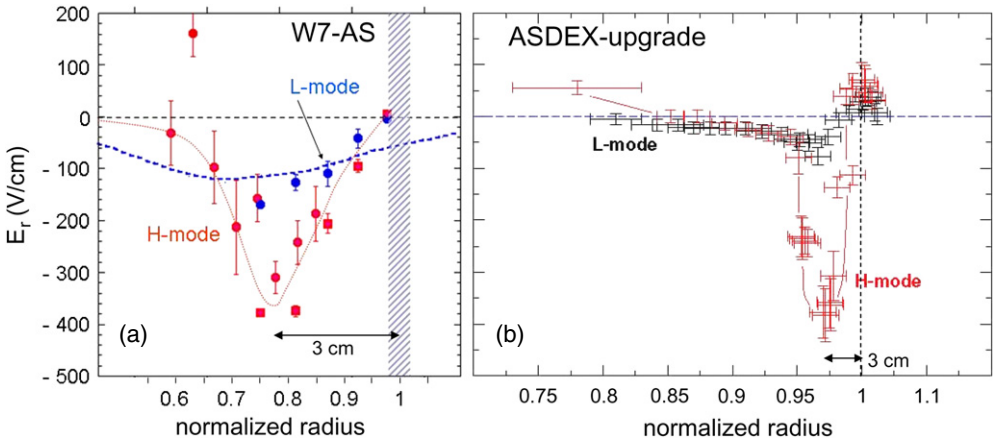

Figure 9. Radial electric field at the plasma edge for W7-AS [43] and ASDEX-Upgrade [45] for L- and H-modes. The radial extent of E_r to its minimum is indicated. For W7-AS the ion pressure gradient is shown as the dashed curve.

inside the separatrix, associated with strong flow shear, is a generic feature of the H-mode. (2) The spatial range of the E_r-field is in both cases 3 cm despite different machine size and thus seems to be governed by local conditions. The overall constancy of the layer width questions models, which strongly involve B_θ. Also the radial extent of the magnetic shear does not seem to play a role. (3) E_r in the L-phase of tokamaks is low and flat [39]; in W7-AS there is already a substantial negative E_r-field in the pre-phase, which is mostly caused by the diamagnetic contribution (dashed curve) and can be well explained by the balance of neoclassical fluxes including the ripple-trapped losses and the off-diagonal terms [44]. In addition, there is no toroidal rotation at the edge of W7-AS owing to the finite toroidal viscosity.

This neoclassical pre-conditioning might be the reason for the low power threshold in W7-AS, which can be below the technical power limits of one source for NBI or one gyrotron for ECRH, respectively—each about 0.4 MW. From the tokamak power threshold scaling [31], more than twice the power is expected.

4.2. Turbulence decorrelation by sheared $E \times B$ flow

The fluctuations residing at the plasma edge close to L–H transitions conditions are resistive ballooning and ion-temperature-gradient driven turbulence. This has been shown for ASDEX-Upgrade in [46] by the analysis of the radial correlation length scaling—in one case with the cell size, in the other one with the ion gyro-radius.

The potential mechanism for the quench of this type of turbulence was developed by Biglari, Diamond and Terry [47]—the decorrelation of turbulent eddies by radially sheared $E \times B$ flow at the plasma edge. Such a mechanism had already been proposed years ago by Lehnert [48]. Substantial evidence has been accumulated that turbulence decorrelation—the reduction of the radial correlation length and the correlation time and the decorrelation of density and potential fluctuations by the sheared flow of the turbulence is indeed the mechanism, which leads to a strongly reduced turbulence level and the formation of a transport barrier. At the TEXT tokamak, the BDT-mechanism was confirmed experimentally, the radial and poloidal correlation times were reduced, the turbulence level decreased and the density gradient increased [49].

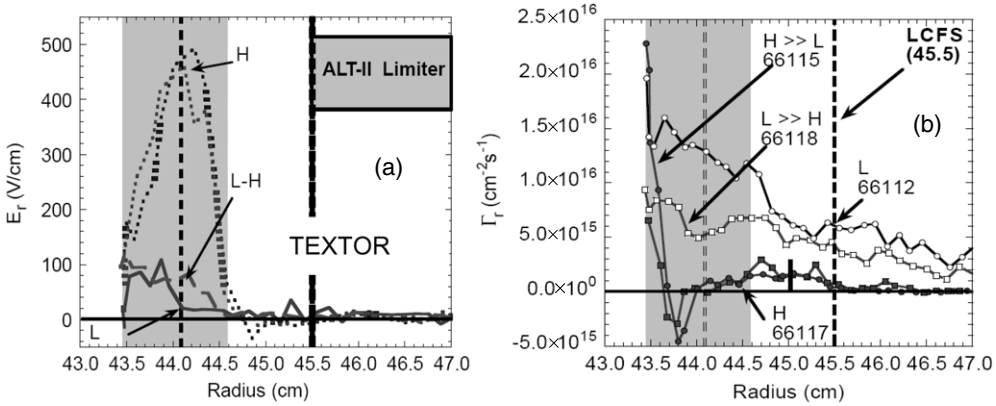

Figure 10. Development of the edge electric field E_r and turbulent particle flux Γ in TEXTOR during biasing experiments. The traces show the L-mode case, the well established H-mode case and the situation right before the L–H transition (marked by L >> H) and before the H–L transition (marked H >> L). The limiter position is shown [51].

Though it is obvious that the E_r-field is strongly affected by the H-transition it is not clear whether the E_r-field is a cause or a consequence of the improved confinement. The use of polarization probes, immersed into the plasma periphery, allowed the radial electric field profile at the edge to be made a control parameter and to study the causality [50]. H-mode transitions could be triggered; the most relevant results were contributed by TEXTOR [51] and the causal relation of sheared flow and turbulence level could be demonstrated in this device [52]. Figure 10(*a*) shows the variation of the edge electric field when the plasma is polarized by a probe which is 4.5 cm inside the limiter bounded TEXTOR plasma. The bifurcation occurs at about 450 V. Plotted are the traces in the L-phase, just at the bifurcation (L–H) and in the deeply developed H-phase. Figure 10(*b*) shows the turbulent particle fluxes for the three time points. The global impact of polarization is predominantly the development of a barrier in particle transport with steep edge gradients. The increase of energy is marginal, however, and ELMs are not present (possibly, the pressure gradient is not large enough or a non-linear bifurcation loop is interrupted by the provision of a static external control parameter).

The critical condition, $\nabla|E_r|$, was found in TEXTOR in the range 50–80 V cm^{-2} [53]; on DIII-D, 50–100 V cm^{-2} [16] and on W7-AS ∼90 V cm^{-2} [42] were observed for spontaneous transitions. $\nabla|E_r|$ can be translated into the critical transition condition—the shearing rate

$$\omega_{E\times B} > \gamma_{\text{lin}}, \tag{1}$$

γ_{lin} being the linear rise time of the turbulence. DIII-D has demonstrated that $\omega_{E\times B} \sim \gamma_{\text{lin}}$ in the L-phase and that the drop of E_r at the H-transition causes $\omega_{E\times B} > \gamma_{\text{lin}}$ fulfilling the decorrelation condition [16]. Also, as predicted by theory, the reduction of the radial correlation length of the edge turbulence within the zone of sheared flow has been demonstrated by DIII-D [16, 54].

Whereas a sharp transition is expected from these considerations as soon as the decorrelation condition is met, the turbulence driven particle flux Γ in TEXTOR is already reduced during the polarization phase prior to the actual transition (see figure 10(*b*) and [53]). In the established H-phase, Γ then nearly disappears completely. The gradual effect of weak shear flow on the turbulence level is in agreement with the observation of an already continuously decreasing fluctuation level in W7-AS (deduced from the scattered power from Doppler reflectometry) prior to the actual H-transition, at the transition the turbulence drops sharply. Furthermore, an increase of turbulence is seen right after the heating pulse has been

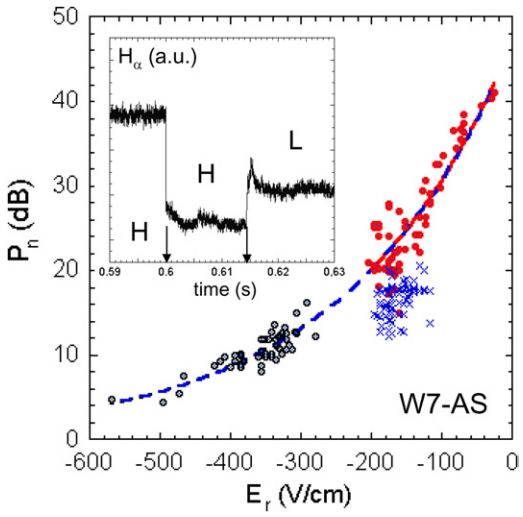

Figure 11. Scattering power of the edge reflectometry system ($n_{\rm probe} = 2 \times 10^{13}\,{\rm cm}^{-3}$; log. plot) of W7-AS versus radial electric field E_r for the phases of the H–L back transition. The gap denotes a jump in E_r. Towards small $|E_r|$, the plasma gradually disappears in the after glow. The crosses show the two parameters at the H–L forward transition. The differences in the two cases close to the respective transitions are caused by the prevailing L-mode profiles in one case and the H-mode profiles (overshoot) in the other. The dashed line is a fit to show how well the two data groups align. Inset: H_α of an H–L back transition; NBI is terminated at the left arrow; the H–L back transitions occurs at the right arrow.

terminated prior to the back transition, followed by a rapid increase at the transition, which is continued by a steady rise up to the gradual disappearance of the plasma in the after glow (as there is no ohmic background heating). Thus, the fluctuation level can be followed at the E_r-well position with E_r varying from $\sim$-600 V cm^{-1} to nearly 0. Such a scan is shown in figure 11. At the H–L transition, E_r jumps (this will be discussed later) and the scattered power P_n (logarithmic scale) further increases. E_r and P_n are measured about 1 cm outside the E_r minimum. The fluctuation level rises by nearly four orders of magnitude. The gap denotes the jump in E_r as shown in figure 15. The smooth but strong relation between P_n and E_r is also indicated by the fit. The fit through both branches hardly differs from that through the individual groups. Nevertheless, there is an asymmetry; the fluctuation level right after the H–L back transition is larger than before the L–H transition (see crosses in figure 11). The major reason may be that the L-phase after the back transition starts with H-mode edge profiles, which transiently overheat the L-mode turbulence whereas the forward transition occurs out of L-mode transport equilibrium conditions. The second asymmetry is that after the L–H transition, the fluctuations completely disappear (in the k-range under investigation: $k_\theta = 6$–$10\,{\rm cm}^{-1}$) whereas they reappear in the H-phase as soon as the heating power has been terminated.

5. The origin of the radial electric field

5.1. The $\nabla p_{\rm i}$-term

The steady-state radial electric field has in its most simple formulation two constituents—the diamagnetic contribution and the $v \times B$ components:

$$E_r = 1/Zen_{\rm e}\nabla p_{\rm i} - v_\theta B_\phi + v_\phi B_\theta, \tag{2}$$

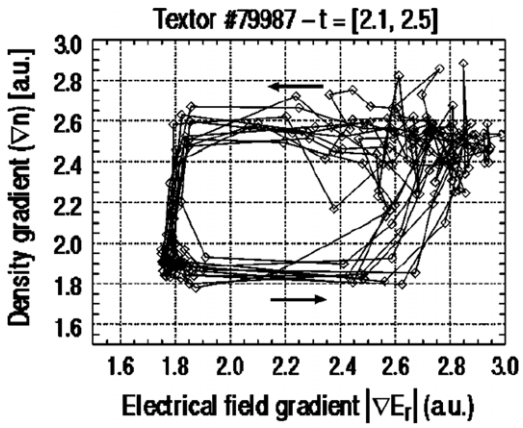

Figure 12. Plotted is the density gradient against the radial electric field during a probe polarization experiment with oscillating field. The analysis shows that E_r leads the cycle by 5 ms. The data are measured at TEXTOR [55]; the plot is taken from [16] (reprinted with the permission of AIP).

∇p_i is determined by the power balance involving heat and particle sources and sinks and—prior to the transition—L-mode transport. There is overall agreement that this component indeed plays a significant role after the H-transition: the ∇p_i—term develops within a confinement time, deepens the E_r—well at the edge and stabilizes the H-mode turbulence decorrelation condition [5, 16, 45]. In the case of ASDEX-Upgrade, the H-mode E_r-field in a developed phase can be explained exclusively by the pressure gradient [45].

Right at the H-mode transition, the situation is different. The time scales involved are much shorter than those of transport and ∇p_i is found to lag behind the rapid development of E_r. Figure 12 shows the result of enforced H-transitions obtained with a biasing probe with oscillating voltage on TEXTOR [55]. The probe gave rise to an oscillating electric field gradient and a modulation of the density. Figure 12 plots the density gradient against the field gradient [16]. It is the field gradient which leads the bifurcation loop and the density gradient—representing ∇p_i—which follows with a delay of about 5 ms. The conclusion from the time lag is that E_r (or E_r', respectively) is obviously the cause of the transition, leading, as a consequence, to an increase in ∇p_i.

5.2. Time scales of transition and transport barrier development

The H-transition, induced by auxiliary heating, has a pre-phase which starts as soon as the heating power has been increased. This phase of formation is shorter in the case of higher heating power, in deuterium instead of hydrogen and with proper ion-grad-B drift. The dwell-times of short H-phases after sawteeth or after beam heating in the phase of the PBP-T_e-rise are in the range of 20 ms. In W7-AS, the pre-phase starts at constant heating power when the density rise has been completed, the plateau is reached and the plasma re-adjusts after the gas-input has been trimmed to the proper level. All these time scales allow the plasma gradients to change.

Also within the H-mode, when the energy content gradually increases and the edge gradients along with it, the development is governed by the confinement time and E_r and ∇p_i develop rather jointly.

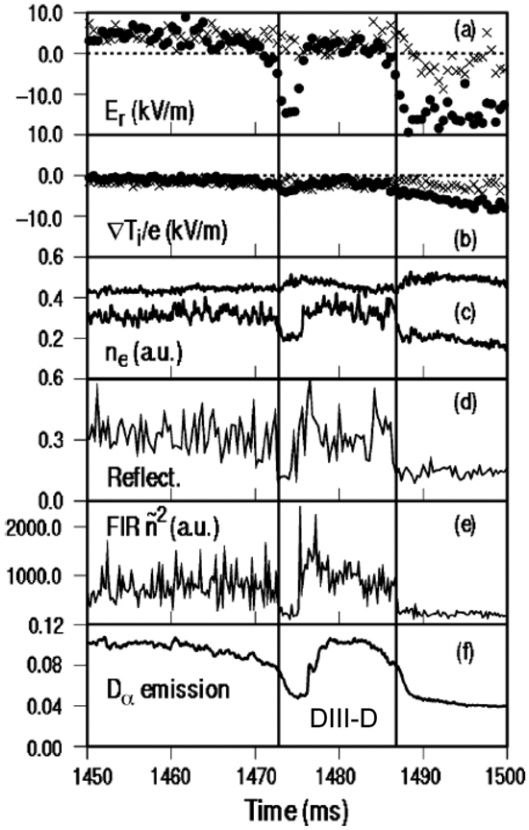

Figure 13. Tableau of a DIII-D H-mode transition with good time resolution. The H-transition has a preceding dither. The first three traces are measured at different edge radii. (*a*) Edge radial electric field; (*b*) edge T_i gradient; (*c*) edge n_e; (*d*) and (*e*) scattering signals to denote the turbulence level; (*f*) D_α. Of importance is the slow pre-phase in E_r prior to and the rapid decrease of E_r at the transitions (in comparison with, e.g. ∇T_i) [35]. Reprinted with the permission of AIP.

The actual transition into the H-mode is governed by a much shorter time scale. Values as short as 12 μs have been measured in JFT-2M for sawtooth initiated transitions [56].

DIII-D closely monitored the H-mode transition with diagnostics with good time resolution. Such a transition is shown in figure 13 [35]. The data show first an L-mode, which transits into a short H-mode, continues with a short L-phase and makes a final H-mode transition. The significance of the plot is the rapid and substantial variation of the electric field in comparison with the slow variation of the ion temperature gradient and the small variation of the density (representing together the ion pressure gradient). The consequence of these studies is that the ion pressure gradient, which deepens the electric field after the transition and stabilizes the H-mode and which is the reservoir for the delayed back transition, does not primarily trigger the H-mode transition. Another mechanism, operating along a short time scale must become effective.

Figure 14 shows the final period of a W7-AS discharge after the NBI heating power has been switched off and the plasma energy content decays. The plasma remains in the H-mode before it suddenly transits back into the L-phase after the dwell-time $\Delta t_{\mathrm{H-L}}$. The confinement

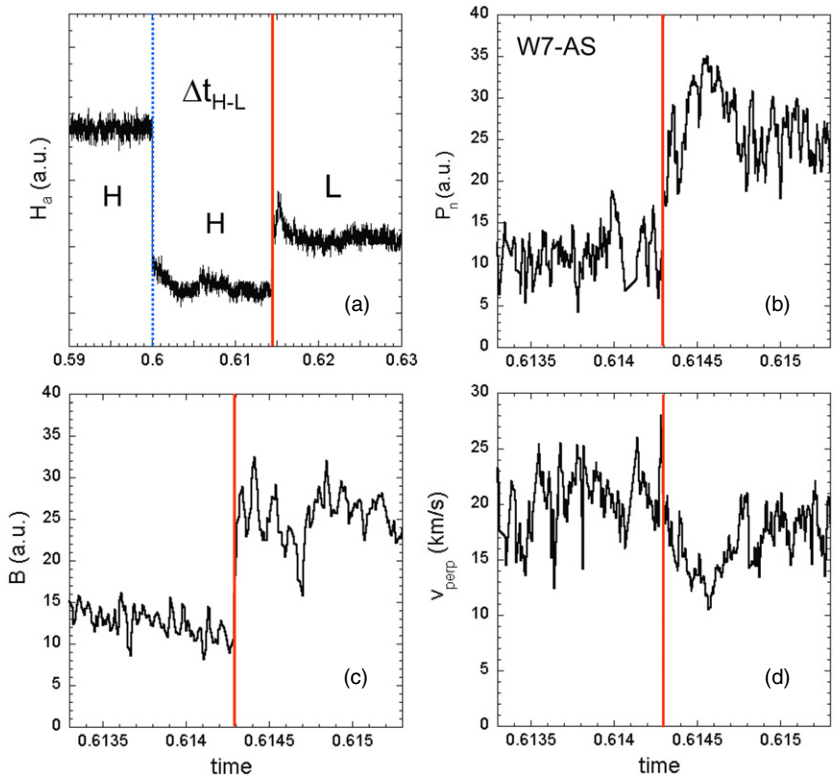

Figure 14. Back transition in W7-AS. (*a*) H_α trace denoting the termination of NBI heating and the H–L back transition. Δt_{H-L} is the duration of the PBP H-phase. (*b*) Reflectometry scattering signal (log. scale); (*c*) Mirnov signal power of fluctuations f $>$ 200 kHz and (*d*) perpendicular flow velocity. The time window of (*a*) is 40 ms; that of the other plots in 2 ms.

time in the successive L-mode drops to about half the value of the H-phase (deduced from $\Delta \mathrm{d}W/\mathrm{d}t$). When the beams are switched off, H_α decreases; the H–L transition is indicated by a rise in H_α (see figure 14(*a*)).

Though the back transition occurs without external drive in a sequence of equilibrium phases, the step from the H-mode back to the L-mode is also distinct. In W7-AS, the magnetic fluctuations increase at the transition in a single step within $\sim$10 μs (figure 14(*c*)). The increase of the scattering power P_n (figure 14(*b*)) can be clearly identified within 200 μs (at a diagnostic time resolution of 4 μs). A better identification of the transition time point is not possible because P_n is modulated as is the perpendicular flow $v_\perp$ (figure 14(*d*)). These observations will be discussed below.

At the back transition, E_r jumps from -240 to $-160\,\mathrm{V\,cm^{-1}}$. The jump occurs within $<$1 ms. Plotted in figure 15 is the E_r-field variation at the field minimum. The E_r-field starts to change at NBI termination whereas the ion pressure gradient stays rather constant up to the H–L-back transition.

The short transition times of O(10 μs) are not the time scale for changes of gradients or related quantities like neoclassical fluxes. It could, however, be the time scale of edge ion collisions, the adjustment of an (non-neoclassical) ambipolar electric field or that of turbulent eddies convected by a few poloidal correlation lengths.

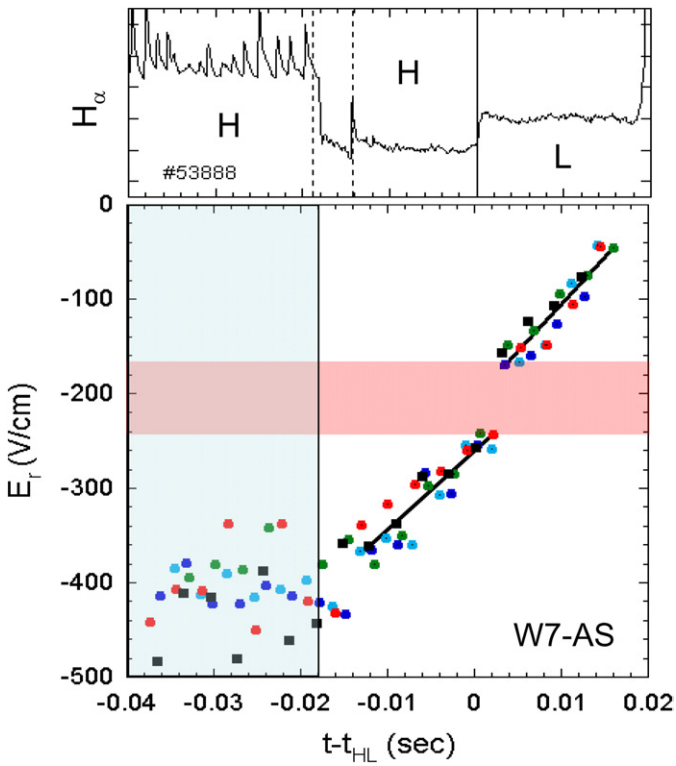

Figure 15. Back transition in W7-AS. H_α denotes the three phases. The H-phase has ELMs; there is also an ELM in the PBP-H-phase. NBI is switched off at the left dashed line. Bottom: E_r is determined for five different discharges (colour-code) from passive CXR spectroscopy (BIV) at the radius of the minimum of the E_r-profile. It is plotted for the three phases: in the H-phase; in the PBP H-phase and at the H–L back transition. Here, E_r jumps within $\Delta t < 1$ ms. E_r further increases towards 0 when the plasma approaches the after glow.

5.3. The $v \times B$ term

The observations reported above show that the $v \times B$ component contributes to the radial electric field and may even be the decisive transition trigger [35]. The $v \times B$ term introduces poloidal and toroidal momentum balances into the transition physics including neoclassical equilibrium characteristics and anomalous transport features. The $v_\phi B_\theta$-term is positive with co-injection and obstructs the development of a negative electric field well. With counter-NBI, the term is negative. Indeed, DIII-D observed that $P_{\rm th}$ is lower in ctr-NBI in comparison with co-NBI [57]. In helical systems v_ϕ is close to zero at the edge owing to the toroidal field ripple; this eases the development of a negative E_r-well.

The inclusion of v_θ into the transition physics opens a rich field of potential transition mechanisms [19]. v_θ is given by the poloidal momentum balance of torques from radial electric currents and poloidal damping (magnetic pumping). The momentum balance is composed of the Lorentz force term, the poloidal damping term, the friction term with the ambient neutrals and the turbulent Reynolds stress term and can be written as

$$0 = j_r B/n_{\rm i} - m_{\rm i}\mu_\theta v_{\theta{\rm i}} - m_{\rm i}\nu_n v_{\theta{\rm i}} + m_{\rm i}\vartheta/\vartheta r(\langle\tilde{v}_{r{\rm i}}\tilde{v}_{\theta{\rm i}}\rangle), \tag{3}$$

j_r is the radial current, μ_θ is the poloidal viscosity, ν_n is the collision frequency with neutrals; $\tilde{v}_{r{\rm i}}$, $\tilde{v}_{\theta{\rm i}}$ are the radial and poloidal fluctuations of the velocity field.

6. Drives for and damping of poloidal flow

6.1. Ion orbit losses

The ion loss-orbit concept [18, 58] for the H-mode is not discussed here in detail because of a lack of space and as it is not the intention of this paper to present a complete overview of potential transition mechanisms [19]. It is based on spontaneous losses of ions; the electron return current $j_{e,r}$ establishes the torque to spin the plasma. One of the attractions of this concept is that it would explain the short transition times. The ion loss model has to be further developed to clarify whether the strong machine-to-machine variation of the edge collisionality ν_i^* at the transition is in agreement with it [3, 7]. Another, possibly conflicting observation is the rather constant width of the edge transport barrier (see figure 9). The restriction of the non-ambipolar losses to energetic instead of the bulk ions may cause problems to apply the model to ohmic or ECR heated plasmas. Also the injection of fast ions into zones of phase space where particles are confined or lost by loss-cone drifts, respectively, did not yield strong support for this model [59]. With respect to the conjecture that the divertor X-point could play a specific role for ion losses, it must be noted that B_θ does not disappear at the X-points in W7-AS.

6.2. The $B \times \nabla B$ drift effect on P_{th}

The flows in the scrape-off layer seem to redistribute momentum and to viscously drag along the plasma inside the separatrix and affect the power threshold giving rise to the $B \times \nabla B$ drift effect on P_{th}. This effect is substantial considering the ratio of $P_{th}^{SN-}/P_{th}^{SN+} \sim 2.6$ for ASDEX (circular cross-section) [7], ~3 for DIII-D (elongated cross-section) [3], ~3.2 for Alcator C-Mod (high-field) [60] and ~3 for MAST (spherical tokamak) [61]. The variation of P_{th} introduced by the shape of the configuration is larger in every device than that allowed by the variation of n_e or B_t, which are scaling parameters of P_{th}. The configurational aspect is the dominant effect. The effect is so massive that a few mm of vertical shift replace MW of heating power.

The v_θ-profile and the radial correlation length of the edge turbulence differ strongly in the zone of the edge shear layer in DIII-D between the two ion-grad-B drift directions [62]. In the low-P_{th} case, a distinct radial reversal of the poloidal propagation of the edge fluctuations is observed, which is not present in the high-P_{th} case. The field reversal increases the shear flow and could be the cause of the lower P_{th} in the SN^+ configuration. These results show that the $B \times \nabla B$ effect has its origin at the plasma edge.

The static SOL parameters in Alcator C-Mod do not vary with the $B \times \nabla B$ direction with respect to the X-point apart from the parallel fluid flow, which shows a strong dependence on configuration [60]. The SOL flow is mostly driven by an asymmetric power exhaust, which is predominantly concentrated at the bad curvature side close to the plasma midplane. A net momentum is imparted to the SOL, which couples across the separatrix and leads to core toroidal rotation [63]. It has to be noted that these studies are carried out with ICRH without an external momentum source. The SOL flow emerges from a different path length from the stagnation point to the outer or the inner sink (target plate), respectively. This weighting leads in the SN^+ case to a net co- and in the SN^- case to a net ctr-flow. In this way, different electric fields are set up in the SOL, which serve as boundary conditions for the E_r-field evolution inside the separatrix. The net-co flow gives rise to a more positive E_r-field in the SOL which might lead to a steeper E_r-field gradient inside the separatrix. Ctr-flow in the SN^- case reduces the E_r-field possibly necessitating more heating power for the H-mode transition.

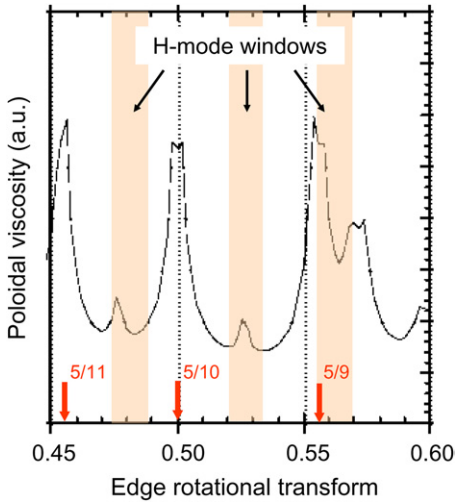

Figure 16. Poloidal viscosity versus edge rotational transform for W7-AS vacuum field conditions [16]. The maxima are linked to the edge island chains which vary in this iota-range from 5/11 to 5/10 to 5/9. The H*-mode windows are linked to the periodic field structure. Two windows are located at the viscosity minima; for the high-iota case good agreement is not found.

In a stellarator with an island divertor such as W7-AS, the flows in the SOL are more fragmented with counter flowing parts which annihilate each other [64]. Therefore, no strong impact of SOL flows on the development of the E_r-field inside the separatrix is expected. Indeed, drift-effects on $P_{\rm th}$ have not been observed.

6.3. The role of the poloidal viscosity

The study of the H-mode boundaries in W7-AS gave strong evidence of the role of neoclassical poloidal damping for the H-mode transition conditions. The H-mode can be realized in W7-AS at a low power threshold but only in isolated iota windows [65] (see figure 16). These windows are periodically linked to the island chains 5/11, 5/10 and 5/9 whose associated chain of natural islands establish the inner separatrix. This close link of periodic magnetic structure and H-mode operational range indicates that the edge magnetic field structure is part of the H-mode transition conditions. This points to the role of a neoclassical mechanism being involved.

Figure 16 shows the neoclassical poloidal damping [66] owing to the specific field Fourier coefficients, which compose the field structure at the edge of W7-AS. The actual value of poloidal damping depends on collisionality and radial electric field; only a specific case is shown. Apart from the high-iota window, the quiescent H-modes develop at the minima of poloidal damping.

Also He-J, an optimized low shear heliotron, observes the H-mode in restricted iota windows [67] but also no perfect match with the minima in poloidal flow damping is achieved. Deviations may be caused by the reference to the vacuum field structure (basis for the results of figure 16); the actual equilibrium with the corrugated island edge structure cannot yet be reconstructed.

Though these results point towards an active role of neoclassical poloidal flow damping (like the effect of toroidal flow damping by perturbation coils on the development of internal barriers), it should also be pointed out that both poloidal neoclassical viscosity and the energy

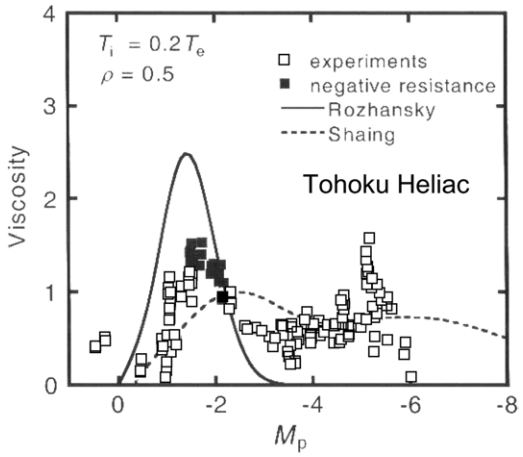

Figure 17. Poloidal viscosity measured in the Tohoku heliac [73] against the poloidal Mach number M_p. The edge flow is varied via an emissive polarization probe. An enforced H-transition occurs between—$M_p = 1$–2. The data are compared with the theories of Rozhansky [72] and Shaing [58].

transfer from zonal flows (ZFs) to geodesic acoustic modes (GAMs) is governed by the geodesic curvature [68, 69]. Therefore, also a mechanism affecting turbulent processes may be behind the observations shown in figure 16. Another conjecture could be the suitable location of low-order rational flux surfaces easing the development of a transport barrier [70]. No analysis in this direction has been done.

The poloidal Mach number M_p of the edge flow of W7-AS is typically in the range of 2–3. As H-mode E_r and edge T_i values are rather similar in fusion devices, one can expect that also tokamaks operate close to this M_p value. Unfortunately, there is no large database available. In this range, the poloidal viscosity shows a sudden decrease as soon as the toroidal resonance has been overcome [71, 72]. In stellarators the resonances linked to the helical ripples additionally play a role [58].

Figure 17 shows the poloidal viscosity μ measured in the Tohoku heliac [73]. The H-mode transition is driven via biasing. Poloidal flows up to and beyond the critical M_θ value are easily possible and indeed the drop in μ is verified. The results have been compared with two theories, one applicable to tokamaks [72] the other to helical systems [58].

6.4. The role of Reynolds stress

The term of the poloidal momentum balance which is most intricately involved in the H-mode transition scenario with the sudden quench of large-amplitude L-mode turbulence is the dynamic Reynolds stress term (4th term on the right hand side of equation (3)). The turbulent Reynolds stress plays an important role in normal fluid dynamics (see below). For two-dimensional flows, the Reynolds stress couples wave energy from smaller scales to larger ones and a mean fluid flow, so-called zonal flows (ZFs) [69], are self-generated out of the turbulence field. The Reynolds stress and its potential to drive flow has nicely been measured by Holland *et al* at the linear plasma device CSDX [74]. Figure 18, top left, shows the radial profile of the measured Reynolds stress emerging from collisional drift waves and figure 18, bottom left, documents the good agreement of the measured mean azimuthal velocity profile generated from the fluctuation field with the expected one. These results of a linear machine show nicely the Reynolds stress generated flows. The same effectiveness cannot be expected

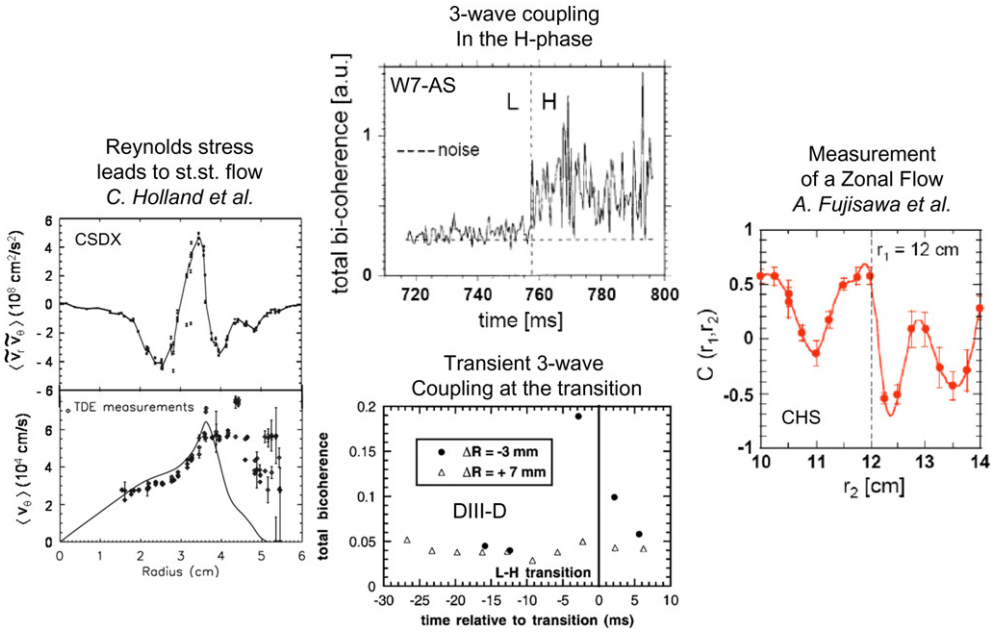

Figure 18. Left column top: Reynolds stress against plasma radius of the CSDX device; bottom: flow induced by the Reynolds stress; the data are compared with theory [74]. Reprinted with the permission of the APS. Middle column: total bi-coherence (three-wave coupling) versus time for L- and H-phases. Top: in W7-AS the bi-coherence is finite in the H-phase [75]. Reprinted with the permission of the American Physical Society. Bottom: ibid DIII-D. L and H-modes are compared. The bi-coherence is transient and large directly at the transition [77]. Reprinted with the permission of AIP. Right: Cross-correlation coefficient C for a fixed reference radius $r_1 = 12\,\mathrm{cm}$ ($\rho = 0.67$). The graph represents the radial potential structure of a ZF. The measurements are carried out with two HIBP at CHS [78]. Reprinted with the permission of the APS.

in toroidal systems because of damping of the associated parallel flows. Therefore, separate measurements in toroidal systems are necessary, in the case of tokamaks specifically at the egde with strong damping due to high q.

The action of Reynolds stress can also be demonstrated by a totally different technique—the analysis of density and velocity fluctuations via bi-coherence spectral analysis as the production of ZFs via the Reynolds stress mechanism is equivalent to three-wave coupling [75, 76]. Figure 18, middle top and bottom, show results from W7-AS [75] and DIII-D [77], which yield a distinct finite bi-coherence in the H-phase, in W7-AS throughout the H-phase, in DIII-D transitorily facilitating the bifurcation before the ∇p_i-term develops and stabilizes the new mode. Also in H-modes induced by biasing, large and steady-state bi-coherence values are observed [76].

Another important element in the chain of self-generated flows is the direct proof of their existence via their electrical potential structure. ZFs are characterized by a strong radial variation of the electrostatic potential with $m = 0$, $n = 0$ poloidal and toroidal topology and a narrow radial correlation. The intrinsic element of a ZF, its potential structure, has been measured by Fujisawa utilizing the double-HIBP installation at the CHS heliotron [78]. Figure 18, right side, shows the radial structure of a ZF deduced from the correlation of potential differences between a fixed reference and various radial positions. The potential amplitude of the ZF is about 1 V, the characteristic radial length is about 1 cm. The ZF feature was measured

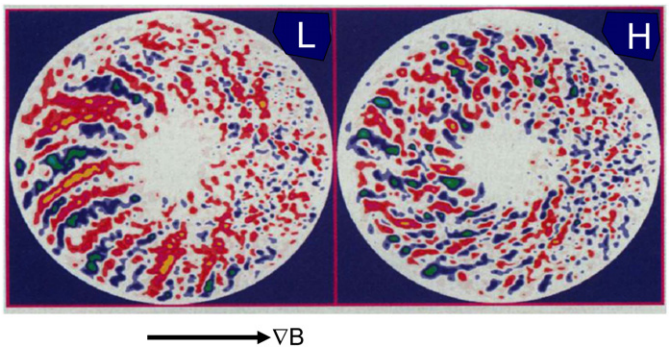

Figure 19. Poloidal contour plots of fluctuating potentials from non-linear global simulations with the flows suppressed (left) and with $E \times B$ flows included (right). ∇B points to the right [79]. Reprinted with permission from AAAS.

at $r/a = 0.67$ (not in the region of the edge transport barrier; therefore, the ZF-amplitude is small). It has to be noted, however, that the q-dependent part of flow damping is easing the development of ZFs at the edge of helical systems (negative shear). In summary, there is good experimental evidence of the action of the Reynolds stress, the existence of ZFs, the formation of ZFs from the turbulence field via three-wave coupling at the plasma edge, relevant to the H-transition.

Global gyro-kinetic numerical models, which simulate the full plasma and allow the self-consistent variation of the pressure profile, can model the turbulence decorrelation by sheared flow [79]. The basis for these simulations is the zonal-flow generation via Reynolds stress from the ambient turbulence field [69] and the turbulence decorrelation via critical shear flow (equation (1)) [47]. The non-linear evolution of the turbulence-zonal-flow system is done on the basis of ITG instabilities in toroidal geometry. Figure 19 shows the potential fluctuations of ITG turbulence with its characteristic prolate structures (due to the intrinsic dia-magnetism of the turbulent eddies) without flow and with self-consistent poloidal flow (the superimposed poloidal flow component is removed for clarity). With flow, the radial correlation length is strongly reduced and the turbulent eddies are nearly isotropic in r and θ.

7. A possible paradigm of the H-mode transition

The understanding of the H-mode transition on the basis of self-induced flows, which annihilate the initial driving mechanism, requires rather detailed knowledge of spatial and temporal structures of the edge turbulence. The Langmuir probe is the only diagnostic which can provide this information. Its safe application requires, however, low power fluxes at the edge. This condition may not necessarily be provided in high-power L-mode discharges, which show the H-mode transition in the most relevant environment. Helical systems can produce plasmas with low heating power. Therefore, they have contributed to the understanding of the H-mode in a rather unique way [26].

In this section, we summarize some of the findings from the H-1 heliac [80]. H-1 operates at low field, low density, with argon plasmas and with a heating power of ∼60 kW. Spontaneous H-mode transitions are observed which double the particle and energy content (see figure 20(a)). The secondary characteristics of the H-mode are provided: sudden, sharp transition, steep edge gradients, a more negative E_r at the edge and the disappearance of turbulence (but no ELMs).

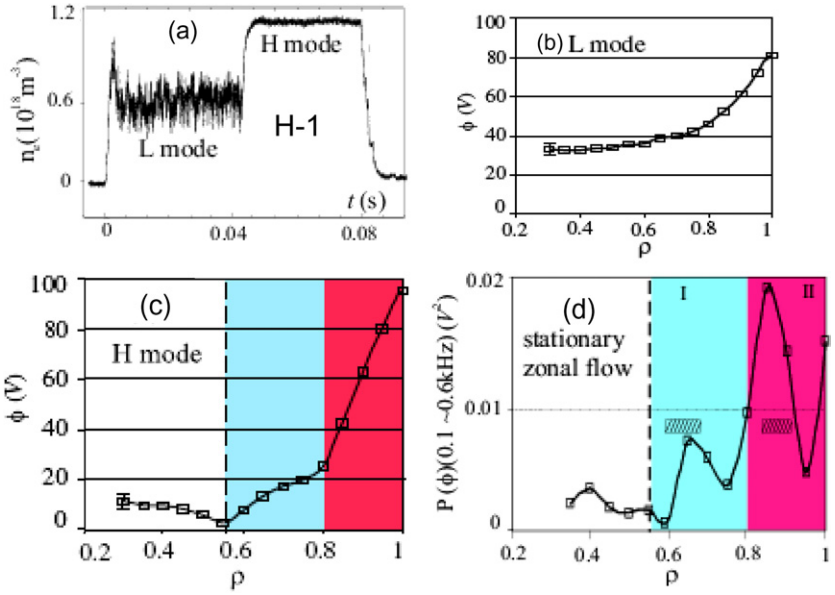

Figure 20. Spontaneous H-transition is shown from the H-1 heliac. (*a*) Plots the density and displays the effect of the transition. (*b*) Potential profile in the L-phase; (*c*) ibid: H-phase; (*d*) radial profile of the spectral power density of stationary ZFs [(0.1–0.6) kHz]. The hatched bars indicate the radial positions of the maximal E_r-values of (*c*) [82]. Reprinted with the permission of the APS.

Figures 20(*b*) and (*c*) show the radial variation of the plasma potential Φ in the L- and the H-modes; figure 20(*d*) shows a low-frequency portion of the spectral power density $P(\Phi)$ (between 0.1 and 0.6 kHz), which displays a strong radial variation [81]. The frequency range is that of ZFs; the mode $m = 0$, $n = 0$ structure has been verified. The hatched areas in figure 20(*d*) are the regions of maximal radial electric field (deduced from figure 20(*c*)) and the spatial co-incidence is indicative of a contribution of the ZFs to the prevailing mean electric field.

The following picture emerges from the studies in H-1 summarized in [82]: drift wave turbulence is caused by the pressure gradient of the L-phase. The linear drift wave instability resides at $k_\mathrm{i} \sim 200\,\mathrm{m}^{-1}$; this mode establishes the injection energy channel for spectral transfer of energy to other k-ranges. Energy cascades from the injection-k value, k_i, to lower and higher k-values by three-wave interaction yielding broad k-spectra in the L-phase. The modes 'condense' via a non-local transfer process, connecting different size scales, into coherent structures and the spectral energy accumulates at the largest possible scale: energy couples from k_i, energized by the pressure gradient, to the $m = 0$ mode. Oscillating ZFs appear, with a structure corresponding to the largest possible system size, the poloidal circumference. The oscillating ZFs, the GAMs, represent a seed for the H-transition.

At the L–H-transition, the turbulence level on both sides of k_i strongly decreases. The drift wave instability remains, however, and even intensifies because the pressure gradient increases. At the transition, the $m = 0$ mode prevails—the remaining sheared flow. The non-local energy transfer connecting different spectral ranges avoids the development of broad-band turbulence and—as a consequence—the plasma confinement improves. It has been confirmed that the kinetic mean flow energy in the H-mode corresponds to the electrostatic energy of the turbulence in the L-mode (within 20%).

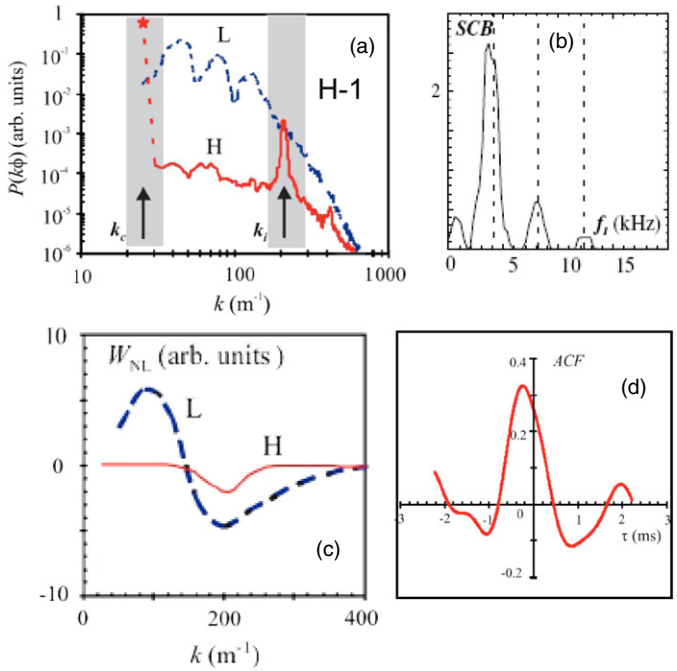

Figure 21. The data are from the H-1 heliac [81,83]. (*a*) Spectra of potential fluctuations in L and H-modes. (*b*) Summed cross bi-coherence (SBC) between different modes in the L-phase. (*c*) Non-linear energy transfer function ($W_{\rm NL}$) of potential fluctuations in L and H modes. (*d*) Amplitude correlation function (ACF) between two $\Delta f = 0.5$ kHz wide bands—one residing at the injection k, $k_{\rm i}$, the other in the k-range of large poloidal structures. Reprinted with the permission of the APS.

Figure 21 summarizes the main experimental evidence for this conjecture [81]. Figure 21(*b*) shows the summed cross-bi-coherence, which is a measure for the coherent 3-wave coupling. The maximum at 4 kHz suggests that the strongest non-linear coupling with other modes is with this low-frequency $k_\theta \sim 0$ mode. In figure 21(*a*), power spectra are plotted, which show that the power drops in the H-phase for all k-values apart from $k_{\rm i}$, where the energy is pumped into the system. The L-mode spectra are plotted close to the transition. At small k, large coherent modes are shown with the $m = 0, 1, 2$ structure. Figure 21(*c*) shows the energy transfer function, which denotes the energy transfer between different k-ranges. At the drift wave pump-k-vector and beyond, energy is lost, which is gained by the lower k-range of the spectrum. Figure 21(*d*) plots the amplitude correlation function whose sign denotes the energy flow between two spectral ranges. This is shown for the H-phase and correlates the injection $k_{\rm i}$ (large k) with the mean ZF (small k). The maximum of the amplitude correlation function resides in the negative time-lag domain, which shows that energy flows in the H-mode from high-frequency (high-k) modes to a zero-frequency (low-k) structure. The actual H-transition is reached when the mean flow shear suppresses the global acoustic modes (GAMs) so that the energy losses from ZFs to GAMs are stopped [83].

The interaction between the turbulence, perpendicular flow and the possible interference with GAMs can also be seen in W7-AS. Figure 22 shows the back transition of the discharge of figure 15 (top) on an ms time scale [42]. The transition is marked by the sudden rise of the Mirnov signal (bottom). At the transition, the perpendicular flow decreases and the fluctuation power increases (log. scale). Unlike the Mirnov trace, the transition in P_n and $v_\perp$ occurs in steps. Both signals, P_n and $v_\perp$s are modulated by 11 kHz. This is the frequency of the GAM at

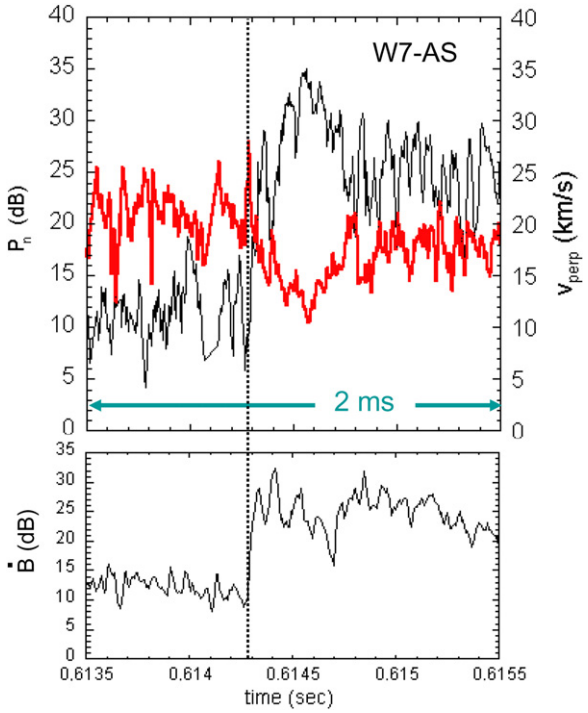

Figure 22. Top: reflectometry scattering signal P_n (thin line, left scale) and perpendicular flow v_{perp} (thick line right scale) at the edge for an H–L back transition (dashed line) of W7-AS [42]. Bottom: Mirnov signal which denotes the transition. P_n and v_{perp} are modulated at 11 kHz presumably by a GAM fluctuation.

the edge of W7-AS. Structural information of this mode is, however, not available. Correlation analysis shows that P_n and $v_\perp$ are anti-correlated prior to the transition: $v_\perp$ increases when P_n decreases. P_n leads this action by 10 μs [84]. This phase relation can be interpreted as evidence for the transfer of spectral power from the turbulence to the flow. More information is necessary, however, to finally conclude this. After the transition, P_n and $v_\perp$ are now correlated and increase or decrease simultaneously. At the transition, the phase relation changes. This relation could be interpreted in the sense that, e.g., the pressure gradient is modulated and this causes P_n and $v_\perp$ to change simultaneously.

Figure 23 shows the back transition now on a 100 μs time scale. The diagnostic, Doppler reflectometry, allows this resolution. The transition is marked and occurs within the two vertical lines. It happens after a strong positive increase of $v_\perp$ when the flow sharply swings back. In this phase the turbulence level is anti-correlated and increases. As the transition happens, the average fluctuation level does not reverse but continues to grow, the average value of $v_\perp$ further decreases and L-mode conditions are established.

8. Turbulence and flows in other physics systems

Though many other ideas on the H-mode transition mechanisms have been generated [19], I have described the one in more detail, which most directly evolves from the causes of degrading confinement with power—the rising fluctuation level of the L-mode. This part of the transition physics—the creation of coherent large-scale flows out of waves and turbulence

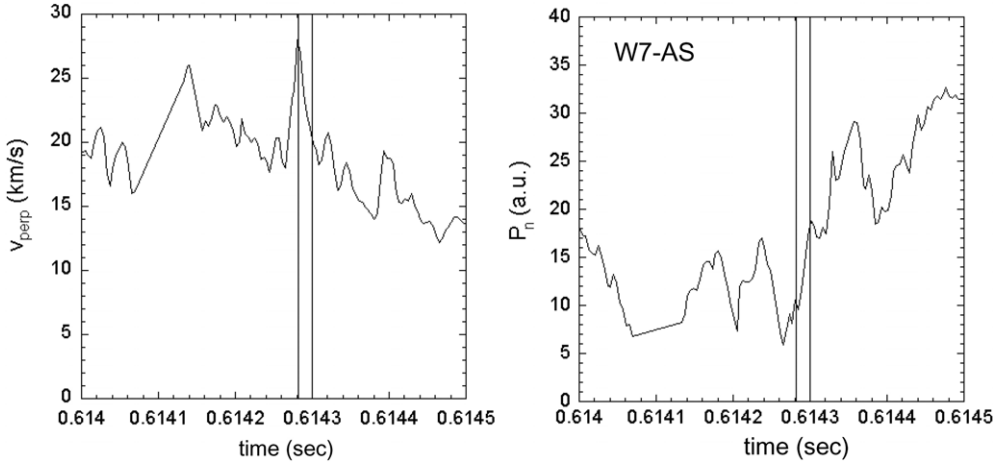

Figure 23. As in figure 22 but for a 500 μs time window. The H–L back transition occurs between the two vertical lines after $v_\perp$ has reached a maximum and P_n starts to rise.

by the Reynolds stress—represents a rather universal mechanism. This process plays a role in Navier–Stokes laboratory experiments [85] and in nature.

Reynolds stress and its gradient as force play an important role in normal fluids and gases in the production of large-scale steady flows, e.g. so-called 'sonic winds' in gases by the rectification of small-scale attenuated waves or turbulent fluctuations. The non-linear interaction of small and large scales with inverse cascading energy flows can feed jets (equivalent to ZFs) as observed in the atmosphere of rotating gaseous planets. Boundaries play an important role for the development of flow vortices and jets. ZFs are observed in the ocean, in the atmosphere, the ionosphere, the sun and in the atmosphere of gaseous planets [86]. In his review, Terry summarizes the physics of sheared flows in rotating (2D) neutral hydrodynamic systems and discusses the analogy to magnetized (2D) plasmas [20].

8.1. Ionosphere

Rossby waves are long-wavelength motions occurring in the ocean, the atmosphere and (as magnetized Rossby waves) in the ionosphere. From the dispersion point of view they are analogous to drift waves in magnetized plasmas. The Coriolis force replaces the Lorentz force. Rossby waves can generate ZFs via Reynolds stress [87].

The meanders of the Gulf stream with a period of about 40 days are affected by Rossby waves. In the atmosphere, Rossby waves give rise to the meandering shape of the Jet stream with the excursions migrating from west to east. When the meanders become very large, they can laterally move large masses of cold or warm air, establishing the meteorology of our daily weather in the northern hemisphere consisting of sequences of low- and high-pressure areas (cyclones and anticyclones). The Rossby wave-ZF system can establish transport barriers and can prevent the lateral mixing of neighbouring layers. They are proposed as a mechanism for the depletion and filling of the ozone hole over Antarctica [88].

8.2. Sun

Whereas the core of the sun (radiative interior) shows solid-body rotation, the convection zone shows sheared flows, e.g. the equator zone rotates with a 25-day and the pole area with about a

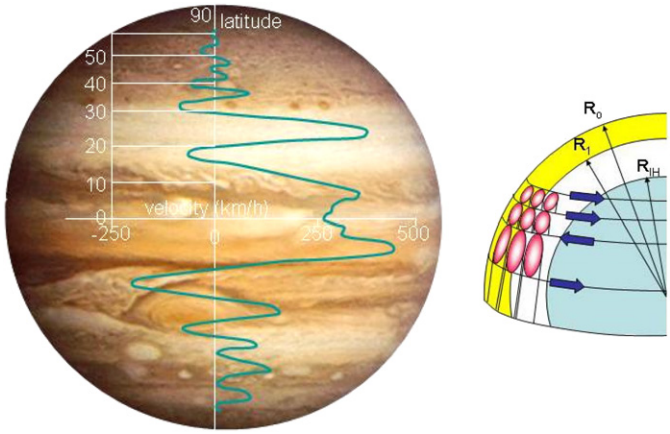

Figure 24. Jupiter with characteristic bands and ZF velocities [92]. Right: shown are schematically convective cells in the outer gaseous layer (between R_0 and R_1), driven by the heat flux from the core, which are conjectured to lead to a macroscopic flow via Reynolds stress [93]. R_{IH} is the assumed radius of the liquid hydrogen core.

35-day period. Strongly temporal and spatial changes in the rotation happen at the tachocline, which separates these radial regions and which is the zone of strong flow shear. Changes in the rotation speed in time have been observed both at the level of the tachocline and the sun surface [89]. Here deep, laterally banded ZFs, so-called torsional oscillations, have been observed with differential rotation to the average rotation velocity.

The amplitude of the ZFs is correlated with the solar activity. Sunspots seem to propagate azimuthally with the migrating torsional oscillations. The flow pattern of the differential rotation within the convection zone has a periodicity, which is half of that of the solar activity cycle (22 years).

8.3. Saturn and Jupiter

The Saturn and Jupiter atmospheres have zones with strongly varying azimuthal velocities. Bands of flows, which rotate with the magnetic field, alternate with those which are much faster propagating to the east (prograde). These stable ZFs are laterally wider close to the equator; the pattern is remarkably north–south symmetric indicating that the driving mechanism resides deeper in the more symmetric core. The generally accepted model for the ZFs is that they are driven by a system of co-axial cylindrical convective cells, which are aligned with the planet's rotation axis and thermally driven by the radially propagating energy flow [90]. Energy and momentum are transmitted from the convective cells to the ZFs by the Reynolds stress.

The different lateral extensions of the ZF band structure of Saturn and Jupiter is explained by the different gravity, which changes the inner boundary providing a relatively thicker atmosphere in the case of Saturn.

Figure 24 shows Jupiter with the lateral variation of the velocity of the ZFs on the left side [91]. On the right side, the modelling geometry is shown with the atmospheric annulus between R_0 and R_1 where the ZF activity occurs [92]. The conjecture is that convective cells driven by the radial heat flux from the core (sketched in figure 24, right) are the origin of the ZFs. The non-linear physics of the model, based on the mechanisms mentioned above, reproduces the major features.

9. Achievements making use of the H-mode

The evolution of the edge pressure profile in the H-mode is limited by striking an MHD instability condition. As a consequence, ELMs appear as a large and violent edge process. All confinement properties (energy, particle, impurities and momentum) are affected. The quiescent H-mode without ELMs has superior confinement, is hampered, however, by rising impurity radiation also from the plasma core. Nevertheless, plasmas with the highest confinement and best performance can be achieved transiently. ELMs contribute, however, also with a positive feature because they purify the plasma, providing constant low-level impurity concentrations and allowing for steady-state operation. There seems to be a milder instability process than ELMs possible at the edge, which also limits the impurity concentration to a tolerable level but avoids the detrimental wall interaction of ELMs. These are quasi-coherent modes, which have been observed in Alcator C-Mod [93] (in the EDA phase), or as edge-harmonic oscillations in DIII-D [94] (in the QH-mode), respectively, and recently also in the HDH-mode [95] of W7-AS [96]. Such edge-conditions may combine important features—good confinement, steady-state capability and benign plasma–wall interaction.

9.1. The 16.1 MW fusion power discharge of JET

JET has achieved 16.1 MW fusion power in the quiescent H-mode for about $0.5\tau_E$ [14]. The DT-mixture was close to 1; $Q = P_{\text{fusion}}/P_{\text{input}} \sim 0.62$; $n_{\text{D}}T_{\text{i}}(0)\tau_E \sim 8.7 \times 10^{20}\,\text{m}^{-3}\,\text{keVs}$. The major traces (including the DT fusion power) of this world-record discharge are shown in figure 25.

9.2. The $Q = 10$ equivalent discharge of DIII-D

The quality of the H-mode has impressively improved since its discovery. At the 2006 IAEA conference, the paper by Luce *et al* [97] received a prize because it presented and discussed a nearly steady-state discharge, which would yield $Q = 10$ when scaled to ITER. The discharge is an ELMy H-mode plasma which is shown in figure 26. The plasma current is 1.2 MA, the field is 1.7 T; $n_{\text{e}} = 0.4 \times 10^{20}\,\text{m}^{-3}$; the heating power is 4.8 MW. The quality parameters of this discharge are $H_{89} = 2.6$, $\beta \sim 3\%$; $\beta_{\text{N}} = 2.7$; $n_{\text{e}}/n_{\text{eGW}} \sim 0, 4$. This state could be maintained for 36 confinement times. Scaled to ITER, this discharge type would allow it to meet its goals.

9.3. The quiescent, quasi-steady-state HDH regime of W7-AS

The overall best performance in W7-AS was achieved in the high-density H-mode (HDH). This mode develops at high-density at a distinct transition, which increases τ_E (if started from the level of normal confinement) and sharply reduces τ_{I}, the impurity confinement time. In this mode, the confinement does not degrade approaching the n_{e}- and beta-limits. For details see [95].

Figure 27 depicts an HDH discharge with $B = 0.9\,\text{T}$, $n_{\text{e}} = 2.5 \times 10^{20}\,\text{m}^{-3}$, $P_{\text{NBI,abs}} = 2.5\,\text{MW}$. The quality parameters of this discharge are: $\beta = 3.4\%$; $\beta_{\text{N}} \sim 9.3$; $H = 1.4$ (related to ISS95-scaling [98]), $n_{\text{e}}/n_{\text{eGW}} = 2.5$, $\tau_{\text{I}}/\tau_E \sim 2$). This quality could be maintained for 85 confinement times.

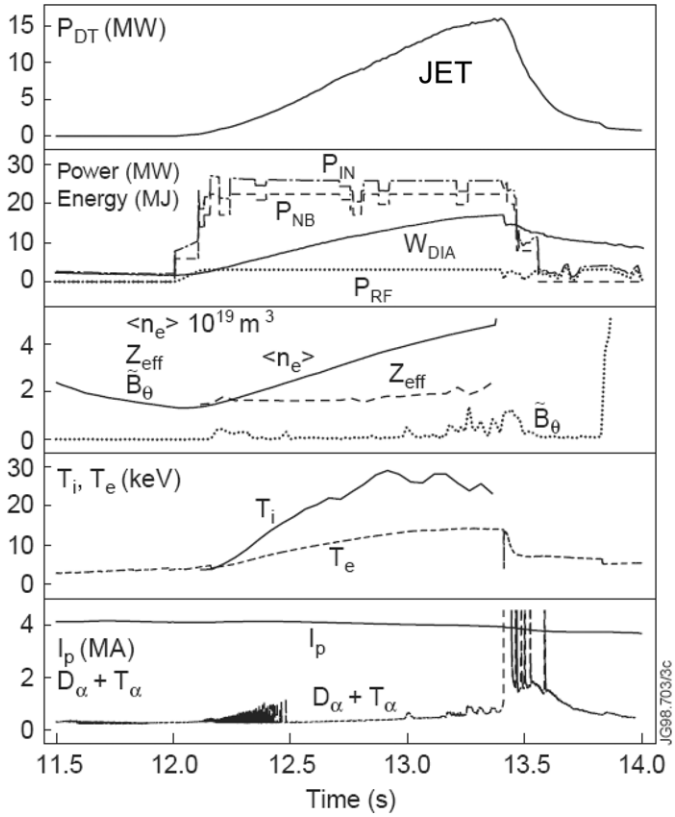

Figure 25. JET H-mode discharge which yielded the highest fusion power (16.1 MW) to date [14].

9.4. The H-mode and ITER costs

Itoh *et al* have analysed the impact of the confinement improvement (in terms of the enhancement factor H over L-mode confinement) on fusion power, Q, and on other parameters [99]. They have also compared the costs of an ITER-like experimental reactor when the targets are reached by a design parameter setting and a plasma size, which are in accordance with L-mode operation or, alternatively, with the improved confinement of the H-mode at a smaller reactor size, respectively. The fusion reactor costs scale like $\$ \sim \mathrm{H}^{-1.3}$. For $H = 2$, the ITER capital costs of 5000 Mill € would increase to 12 300 Mill € for a similarly targeted device based in the L-mode. The savings are substantial.

9.5. The H-mode in a DEMO

Several DEMO designs are available [100]. They all show that τ_E expected from H-mode confinement is sufficient for a reactor power of about 3 GW. The major difference with respect to ITER is a substantially larger β_N and a higher P/R_o (power versus major radius) ratio. Higher β_N will ensure a larger bootstrap current. As the H-mode is characterized by broad pressure profiles, it provides better conditions for more stability at broader current profiles. The higher P/R_o ratio may demand, however, low-fluctuation edge-conditions and may necessitate quiescent, non-ELMy H-modes.

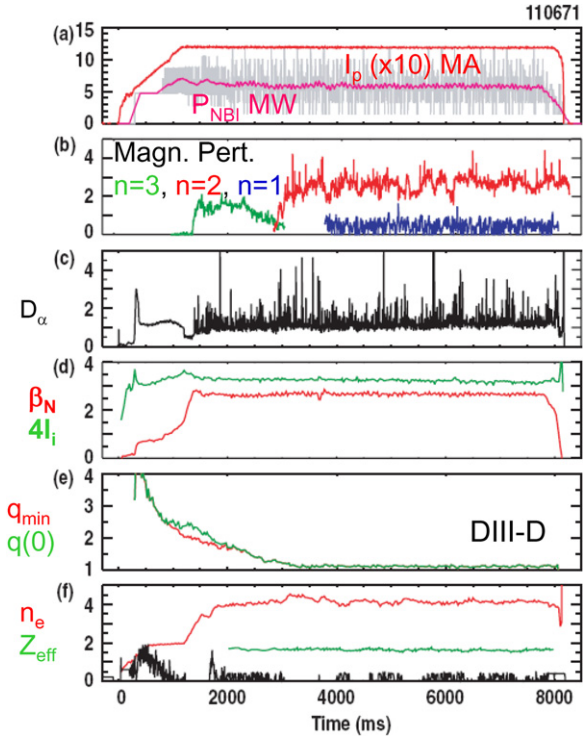

Figure 26. High-performance, long-pulse discharge from DIII-D. This discharge, when scaled to ITER, would qualify for $Q = 10$ operation—the major goal of ITER. Author, team and discharge received a prize at the 2006 IAEA conference [97].

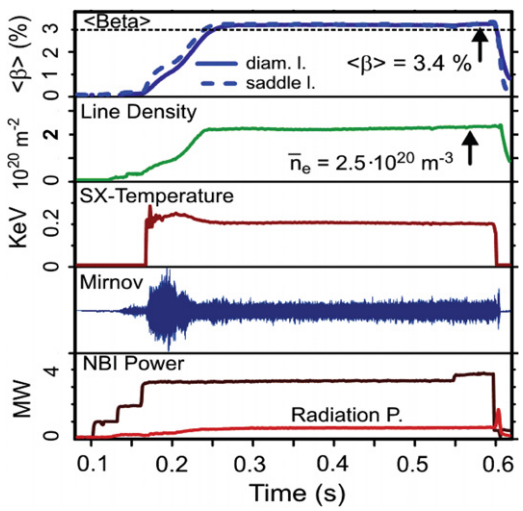

Figure 27. High-performance, long-pulse discharge from W7-AS in the HDH regime [95].

10. Final comments

Confinement in fusion devices obviously develops in two branches. In the L-mode branch, the free energy of the high pressure plasma leads to an increase of the overall turbulence level. A distinct bifurcation is possible, which could emerge in a self-organized fashion: the energy in the 2D-turbulence field spectrally cascades to macroscopic scales giving rise to a mean flow (ZFs or GAMs), which acts back as its radial shear decorrelates the prevailing turbulence. This leads to the H-mode branch characterized by a very low level of edge turbulence in the medium k-range. The energy content of the plasma rises as a consequence and—what might be rather surprising for a thermodynamic system—the self-organizing process brings the plasma closer to ignition conditions. The pressure profile, which is the corollary of the improved confinement, maintains the sheared flow conditions and stabilizes the H-mode.

In stellarators, the H-mode develops basically with the same characteristics, which demonstrates the ubiquitous character of this regime. The neoclassical ambipolar electric field provides good starting conditions for the self-generated flow to ultimately reduce the turbulent fluxes and restore plasma transport closer to the lower-dissipation neoclassical flux level.

The distinct characteristics of the L- to H-transition have contributed to a much better understanding of plasma turbulence and bifurcation mechanisms. Nevertheless, the situation seems to be rather involved. In order to meet the turbulence decorrelation conditions (equation (1)), the power balance has to be evoked together with the toroidal momentum balance, the poloidal flow balance and—because the viscosity associated with the flows on the open field lines of the SOL transfer momentum to the edge plasma—also the scrape-off-layer momentum balance. Many mechanisms with the potential to drive edge flow or to damp it, respectively, interact and define the actual edge flow and decorrelation conditions. The empirical recipes for how to get the H-mode, how to switch from ELMy to the quiescent H-mode and how to expand its operational range have hardly any obvious relation to the transition condition given in equation (1). But the disparity between the simple operational progress on one side and the years it takes to come to a complete understanding on the other might be the best evidence for many detailed mechanisms acting together.

The discovery of the H-mode led to an exemplary international cooperation. Each major toroidal device had the ambition to also operate in this regime and to contribute to its understanding. An important role was played by the bi-annual H-mode workshop and the publication of its results in PPCF. The workshop was initiated by the DIII-D team; the first one was held in 1987 in San Diego; the 11th one was held in 2007 in Tsukuba.

The H-mode research also represents a contribution of high-temperature plasma physics to the understanding of the dynamic behaviour of highly non-linear hydrodynamic systems.

Let me finish with a quote from Hannes Alfvén taken from his Nobel Prize lecture. He says:

> For the non-specialists four-dimensional relativity theory, and the indeterminism of atom structure have always been mystic and difficult to understand. I believe that it is easier to explain the 33 instabilities in plasma physics ...

We should make every effort to prove that Hannes-Alfvén, our only Nobel Prize winner, is correct with this statement. Therefore, I would suggest that we make the H-mode transition physics again part of our experimental programme. There are still many open issues, the time scales, the actual transition trigger, the role of the SOL and the high edge poloidal Mach numbers .... If the only progress is a contribution to the basic understanding of confinement it is fine. But also a better understanding of the power threshold and the edge pedestal physics might emerge.

Acknowledgments

In my professional career I benefited for my scientific interests in magnetic confinement from many fine colleagues. It is a pleasure to thank specifically P Diamond, M Hirsch, S-I and K Itoh, K Lackner, H Maassberg, U Stroth and H Wobig. It was a special privilege to work with the ASDEX and the W7-AS teams.

I want to thank all those who have allowed me to use their figures and specifically M Hirsch for some of the as yet unpublished material.

I would like to thank the Board of the Plasma Physics Division for the honour of this award. I am aware that the prestige of the Hannes-Alfvèn Prize was founded by the previous prize winners, and I am also aware that other deserving plasma physicists will not receive this prize because they are no longer with us, like Boris Kadomtsev, Harald Furth, Derek Robinson, Masahiro Wakatani and many others I could equally well mention—plasma and fusion scientists who have laid the groundwork of our discipline.

References

[1] Wagner F *et al* 1982 *Phys. Rev. Lett.* **49** 1408
[2] Zhao K J *et al* 2006 *Phys. Rev. Lett.* **96** 255004
[3] Carlstrom T N and Groebner R J 1996 *Phys. Plasmas* **3** 1867
[4] Keilhacker M *et al* 1984 *Plasma Phys. Control. Fusion* **26** 49
[5] Wagner F *et al* 1991 *Proc. 13th Int. Conf. on Plasma Physics and Controlled Nuclear Fusion Research 1991 (Washington DC, 1990)* vol 1 (Vienna: IAEA) p 277
[6] Wagner F *et al* 1985 *Nucl. Fusion* **25** 1490
[7] ASDEX team 1989 *Nucl. Fusion* **29** 1959
[8] Steinmetz K *et al* 1987 *Phys. Rev. Lett.* **58** 124
[9] Kaye S M *et al* 1984 *J. Nucl. Mater.* **121** 115
[10] Burrell K H *et al* 1987 *Phys. Rev. Lett.* **59** 1432
[11] Tanga A *et al* 1987 *Nucl. Fusion* **27** 1877
[12] Erckmann V *et al* 1993 *Phys. Rev. Lett.* **70** 936
[13] Wagner F *et al* 1994 *Trans. Fusion Technol.* **27** 32
[14] Keilhacker M *et al* 1999 *Nucl. Fusion* **39** 209
[15] Ikeda K *et al* 2007 *Nucl. Fusion* **47** S1
[16] Burrell K H 1999 *Phys. Plasmas* **6** 4418
[17] Carlstrom T N 2005 *Fusion Sci. Technol.* **48** 997
[18] Itoh K and Itoh S-I 1996 *Plasma Phys. Control. Fusion* **38** 1
[19] Connor J W and Wilson H R 2000 *Plasma Phys. Control. Fusion* **42** R1
[20] Terry P W 2000 *Rev. Mod. Phys.* **72** 109
[21] Hugill J 2000 *Plasma Phys. Control. Fusion* **42** R75
[22] Rozhansky V 2004 *Plasma Phys. Control. Fusion* **46** A1
[23] Hahm T S 2002 *Plasma Phys. Control. Fusion* **44** A87
[24] Wagner F *et al* 2005 *Phys. Plasmas* **12** 072509
[25] Okamura S *et al* 2004 *Plasma Phys. Control. Fusion* **46** A113
[26] Wagner F *et al* 2006 *Plasma Phys. Control. Fusion* **48** A217
[27] Hinton F L 1985 *Nucl. Fusion* **25** 1457
[28] Eubank H *et al* 1997 *Proc. 7th Int. Conf. on Plasma Physics and Controlled Nuclear Fusion Research 1979 (Innsbruck, 1978)* vol 1 (Vienna: IAEA) p 167
[29] Bessenrodt-Weberpals M *et al* 1993 *Nucl. Fusion* **33** 72
[30] Righi E *et al* 1999 *Nucl. Fusion* **39** 309
[31] Snipes J A *et al* 2000 *Plasma Phys. Control. Fusion* **42** A299
[32] Wagner F *et al* 1984 *Phys. Rev. Lett.* **53** 1453
[33] Manso M E 1993 *Plasma Phys. Control. Fusion* **35** B141
[34] Holzhauer E and Dodel G 1990 *Rev. Sci. Instrum.* **61** 2187
[35] Moyer R A *et al* 1995 *Phys. Plasmas* **2** 2397
[36] Zohm H *et al* 1994 *Phys. Rev. Lett.* **72** 222

[37] Itoh S-I *et al* 1991 *Phys. Rev. Lett.* **67** 2485
[38] Itoh S-I and Itoh K 1988 *Phys. Rev. Lett.* **60** 2276
[39] Burrell K H *et al* 1992 *Plasma Phys. Control. Fusion* **34** 1859
[40] Groebner R J, Burrell K H and Seraydarian R P 1990 *Phys. Rev. Lett.* **64** 3015
[41] Field A R *et al* 1992 *Nucl. Fusion* **32** 1191
[42] Hirsch M *et al* 2006 *Plasma Phys. Control. Fusion* **48** S155
[43] Baldzuhn J *et al* 1988 *Plasma Phys. Control. Fusion* **40** 967
[44] Ehmler H *et al* 2003 *Nucl. Fusion* **43** L11
[45] Schirmer J *et al* 2006 *Nucl. Fusion* **46** S780
[46] Kurzan B *et al* 2000 *Plasma Phys. Control. Fusion* **42** 237
[47] Biglary H, Diamond P H and Terry P W 1990 *Phys. Fluids* B **4** 1385
[48] Lehnert B 1966 *Phys. Fluids* **9** 1367
[49] Ritz Ch P *et al* 1990 *Phys. Rev. Lett.* **65** 2543
[50] Taylor R J *et al* 1989 *Phys. Rev. Lett.* **63** 2365
[51] Weynants R R *et al* 1992 *Nucl. Fusion* **32** 837
[52] Boedo J *et al* 2000 *Nucl. Fusion* **40** 1397
[53] Weynants R R *et al* 1998 *Plasma Phys. Control. Fusion* **40** 635
[54] Jakubowski M, Fonck R J and McKee G R 2002 *Phys. Rev. Lett.* **89** 265003-1
[55] Jachmich S *et al* 1998 *Plasma Phys. Control. Fusion* **40** 1105
[56] Ido T *et al* 2002 *Phys. Rev. Lett.* **88** 055066
[57] Gohil P *et al* 2008 *Plasma Phys. Control. Fusion* submitted
[58] Shaing K C 1996 *Phys. Rev. Lett.* **76** 4364
[59] Burrell K H *et al* 2004 *Plasma Phys. Control. Fusion* **46** A165
[60] LaBombard B *et al* 2004 *Nucl. Fusion* **44** 1047
[61] Meyer H *et al* 2006 *Nucl. Fusion* **46** 64
Biewer T *et al* 2006 *33rd EPS Conf. on Plasma Physics (Rome, Italy)* vol 30I (ECA) P-5.112
[62] Fenzi C *et al* 2005 *Phys. Plasmas* **12** 062307
[63] Rice J E *et al* 2005 *Nucl. Fusion* **45** 251
[64] Feng Y *et al* 2006 *Nucl. Fusion* **46** 807
[65] Hirsch M *et al* 2000 *Plasma Phys. Control. Fusion* **42** A231
[66] Wobig H and Kisslinger J 1995 *Plasma Phys. Control. Fusion* **37** 893
[67] Sano F *et al* 2004 *Fusion Sci. Technol.* **46** 288
[68] Winsor N *et al* 1968 *Phys. Fluids* **11** 2448
[69] Diamond P H, Itoh S-I, Itoh K and Hahm T S 2005 *Plasma Phys. Control. Fusion* **47** R35
[70] Estrada T *et al* 2007 *Nucl. Fusion* **47** 305
[71] Shaing K C and Crume E C Jr 1989 *Phys. Rev. Lett.* **63** 2369
[72] Rozhansky V and Tendler M 1992 *Phys. Fluids* B **4** 1626
[73] Kitajima S *et al* 2004 *Proc. 20th Int. Conf. on Plasma Physics and Controlled Nuclear Fusion Research 2004 (Vilamoura, Portugal)* (Vienna: IAEA) EX/9-3
[74] Holland C *et al* 2006 *Phys. Rev. Lett.* **96** 195002
[75] Diamond P H *et al* 2000 *Phys. Rev. Lett.* **84** 4842
[76] Tynan G R *et al* 2001 *Phys. Plasmas* **8** 2691
[77] Moyer R A *et al* 2001 *Phys. Rev. Lett.* **87** 135001
[78] Fujisawa A *et al* 2004 *Phys. Rev. Lett.* **93** 165002
[79] Lin Z *et al* 1998 *Science* **281** 1835
[80] Hamberger S M *et al* 1990 *Fusion Technol.* **17** 123
[81] Xia H *et al* 2006 *Phys. Rev. Lett.* **97** 255003
[82] Shats M G *et al* 2005 *Phys. Rev.* E **71** 046409
[83] Shats M G and Solomon W M 2002 *Phys. Rev. Lett.* **88** 045001
[84] Endler M 2007 private communication
[85] Shats M G *et al* 2007 Private Communication
[86] Marcus P S and Kundu T 2000 *Phys. Plasmas* **7** 1630
[87] Shukla P K and Stenflo L 2003 *Phys. Lett.* A **307** 154
[88] Nishii K and Nakamura H 2004 *Geophys. Res. Lett.* **31** 1
[89] Hughes D, Rosner R and Weiss N (ed) 2007 *The Solar Tachocline* (Cambridge: Cambridge University Press)
[90] Busse F H 1976 *Icarus* **20** 255
[91] Ingersoll A P and Pollard D 1982 *Icarus* **52** 62
[92] Heimpel M *et al* 2005 *Nature* **438** 193

[93] Mazurenko A *et al* 2002 *Phys. Rev. Lett.* **89** 225004
[94] Burrell K H *et al* 2001 *Phys. Plasmas* **8** 2152
[95] McCormick K *et al* 2001 *Phys. Rev. Lett.* **89** 015001
[96] Belonohy E *et al* 2007 *34th EPS Conf. on Plasma Physics (Warsaw, Poland)* submitted
[97] Luce T *et al* 2003 *Nucl. Fusion* **43** 321
[98] Stroth U *et al* 1996 *Nucl. Fusion* **36** 1063
[99] Itoh K, Itoh S-I and Fukuyama A 1992 *Fusion Eng. Des.* **15** 297
[100] Lackner K 1998 *Plasma Phys. Control. Fusion* **40** 557